Investigation of Mechanical Properties, Porosity and Geometric Deviation of Lattice Structures Manufactured by Additive Manufacturing

by

Xiuhui Li

A thesis submitted in partial fulfillment of the requirements for the degree of

Master of Science

Department of Mechanical Engineering
University of Alberta

Abstract

This thesis reports fabrication, mechanical characterization, finite element modeling, and geometric analysis of lattice structures. A net-shaped 316L stainless steel lattice structure composed of diamond unit cells was fabricated by selective laser melting (SLM). The cavities in the lattice structure were then filled by aluminum through vacuum-assisted melt infiltration to form the bimetallic composite. The bulk aluminum sample was also cast using the same casting parameters for comparison. The compressive and tensile behavior of 316L stainless steel lattice, bulk dissolvable aluminum, and 316L stainless steel/dissolvable aluminum bimetallic composite is studied. Comparison between experimental, finite element analysis (FEA), and digital image correlation (DIC) results are also performed. There is no notable difference in the tensile behavior of the lattice and bimetallic composite because of the weak bonding in the interface between the two constituents of the bimetallic composite, limiting load transfer from the 316L stainless steel lattice to the dissolvable aluminum matrix. However, the aluminum matrix is vital in the compressive behavior of the bimetallic composite. The dissolvable aluminum showed higher Young's modulus, yield stress, and ultimate stress than the lattice and composite in both tension and compression tests, but much less elongation. Moreover, FEA and DIC have been demonstrated to be effective and efficient methods to simulate, analyze, and verify the experimental results.

In addition, this thesis also provides a geometric deviation analysis of lattice-based compression and tension samples manufactured with 316L and 17-4PH stainless steel, with different volume fractions (28% and 70%) using laser powder-bed fusion (LPBF). LPBF is widely accepted for manufacturing metal parts with complicated structures. However, LPBF has inherent limitations such as internal porosities and residual stresses leading to size and shape deviations. Thus, a non-

destructive characterization using X-ray microscopy was conducted to collect data. Shape, position, volume, and statistical distribution of porosities and internal defects were characterized. The data was further utilized to conduct a size and shape deviation analysis.

Prefaces

This thesis is an original work by Xiuhui Li. Research work conducted for this thesis have been published in reputed journals and conference publications. Articles which are published or in peer review included are listed below with the corresponding chapter in this thesis.

1. **Li X.**, Ghasri-Khouzani M., Bogno A.A., Liu J., Henein H., Chen Z., Qureshi A.J., "Investigation of compressive and tensile behavior of stainless steel/dissolvable aluminum bimetallic composites by finite element modeling and digital image correlation", Materials Journal, Vol. 14, Issue 13, 2021. https://doi.org/10.3390/ma14133654	Chapter 1 Chapter 2 Chapter 3 Chapter 5
2. Ghasri-Khouzani M., **Li X.**, Bogno A.A., Chen Z., Liu J., Henein H., Qureshi A.J., "Fabrication of aluminum/stainless steel bimetallic composites through a combination of additive manufacturing and vacuum-assisted melt infiltration casting", Journal of Manufacturing Processes, Vol. 69, pp. 320–330, 2021. https://doi.org/10.1016/J.JMAPRO.2021.07.047	Chapter 1 Chapter 2
3. B.S. Rupal, **X. Li**, H.R.Z. Rajani, Z. Chen, A.J. Qureshi, "Porosity and shape deviation analysis of lattice structures manufactured using laser powder bed fusion process", Procedia CIRP, 2022. In peer review.	Chapter 1 Chapter 4 Chapter 5

Apart from publications mentioned above, this thesis also contributed to the following paper:

1. Mostafa K.G., Momesso G.A., **Li X.**, Nobes D.S., Qureshi A.J.,

   "Dual graded lattice structures: Generation framework and mechanical properties characterization",

   Polymers Journal, Vol. 13, Issue 9, pp. 1–28, 2021.

   https://doi.org/10.3390/polym13091528

Acknowledgements

Firstly, I would like to show my sincerest thanks towards my supervisors Dr. Zengtao Chen and Dr. Ahmed Qureshi. Without their guidance, advice and supervision, this work would never reach to such a success. During those hard times in researching, Dr. Chen and Dr. Qureshi have immensely supported and guided me. Thank you for all your time and kind support.

Thanks also to Dr. Hani Henein for your precious suggestion to my work related to chemical and material engineering.

I am also extremely grateful to my great seniors Dr. Baltej Singh Rupal, Khaled Mostafa, and Dr. Morteza Ghasri. Thank you for all of your leading, advice, and supervision when I was stuck in my work and could not find a way out.

Special thanks to my workmates and friends, Shiyu Teng, Weilin Yang, Wenzhi Yang, Saadman Sakib Rahman, Ali Mulhi, Ezz Ahmed, Gowtham Boyala, Janmejay Rao, Michael Kwak, Muhammad Bilal, Remy Samson, and Maha Ead. Thank you for all of your help and support when I am in need. The friendship with all of you helped me quickly adjust and get used to my new life.

I want to thank my best friends, Jiaqi Zhang and Liwei Yu, who gave me the most spiritual encouragement and support even you are residing far away in China. I am grateful that you are

always there when I need any help.

I would like to thank my friends Jiaxing Li, Xiaolan Gao, Haochen Zhang, Yicong Wang, Junpeng Huo, and Linkun Chen in Edmonton. It is always great to spend my spare time with the accompany of my friends. I will never forget the time we spent in Edmonton, a beautiful city nurturing me and will always be regarded as my hometown in Canada.

I am incredibly grateful to my husband, Yue Wu, for being so supportive throughout my study and my life. Your presence shed light on my future path, and I am excited that you will be with me anyhow for the rest of my life.

I am also immensely grateful to my mother for being my pillar of strength. Your support has made me reach the place where I am today and should never be ignored.

Finally, thanks to the Mechanical Engineering Department and the University of Alberta. Thank you for giving me a chance and the best place to study, and any work-related help.

Table of Contents

List of Tables

List of Figures

CHAPTER 1

INTRODUCTION

Additive manufacturing (AM) has become well-known in recent years as a kind of advanced manufacturing technology for its capability to fabricate components with complex geometry through a bottom-up approach of material deposition from powder feedstock. Metal additive manufacturing (MAM) is one type of the AM methods for 3D printing of metallic parts. Among the complex features or structures, lattice structures have gained wide attention due to their lightweight and multi-functional properties, which can be additively manufactured through specific procedures.

In this chapter, AM, lattice structures and the types of unit cells as their components, the bimetallic composite based on the metal lattice structure, as well as the defects of additively manufactured parts and X-ray computed tomography, have been introduced through a comprehensive literature review. The objectives and scope of the research were also elucidated at the end of this chapter.

1.1 Additive Manufacturing of Lattice Structures

The manufacturing method of lattice structures has received widespread attention with metal additive manufacturing (MAM) being a feasible option given the complexity of the geometry. MAM can directly print a geometry layer by layer on a substrate from the bottom to up by metal material feedstock. The sample can be printed from a computer-aided design (CAD), although there are some limitations of samples to be printed in terms of size and geometry for different machines. Selective laser melting (SLM) is one of the categories of MAM. In SLM, several thin

layers of fine metal powder are evenly distributed on a substrate building plate using a coating mechanism. Then, each layer of the component shape is fused by selectively melting the powder, which is achieved with a high-power laser beam. Researchers did some investigation on the defects of the additively manufactured structures. It was noted that struts waviness, oversizing or thickness variation is prevailing on lattice structures fabricated by SLM [1–6] with horizontal struts showing more serious geometric imperfections than vertical and diagonal struts [1, 4, 6, 7]. Moreover, vertical struts manufactured were thinner than nominal as-designed ones [1, 2, 4], and the failure mode will be transferred from one to another with strut oversizing [1]. SLM parameters also affect the mechanical properties of lattice structures [8, 9]. Horizontal struts always start to fracture firstly, which shows the fact that they are undertaking more stress than other struts [6, 10].

Evidence shows that stainless steel lattice structures manufactured through SLM have excellent mechanical performance despite of some structural flaws [11]. Ultrastructure and mechanical property evaluation of duplex stainless steel UNSS31803 treated by SLM was performed by Hengsbach et al. [12]. In addition to duplex stainless steel, 316L stainless steel also has been favored by researchers for their deformation behaviors and mechanical properties, which were studied in [13, 14], and[8].

1.2 Unit Cell of Lattice Structures

Lattice structures have attracted extended attention of many researchers due to their superior properties such as light weight, high strength, high energy absorption, reduced material consumption, and biocompatibility. Lattice structures can be formed mathematically or geometrically by spatial arrangement and combination of a group of unit cells. Most researchers focused on the mechanical properties of unit cells, such as compression and tension behavior [8,

15–21], fracture behavior [1, 22], fatigue behavior [23, 24], and shear response [25], and biocompatibility [26–28]. Research has also been dedicated to design methods of lattice structures, including creating functionally graded porous structures [17, 29–31], panel or sandwich-shaped lattice structures [32–34], and the designing algorithm [35–40].

The mechanical properties of lattice structures mainly depend on the relative density and the number of unit cells presented in lattice structures [41–43]. Relative density is the density ratio of the lattice structure to the bulk material from which the lattice structure is made [43]. The relative density of a lattice structure is equivalent to the relative density of a unit cell if the size and shape of unit cells contained in the lattice structure are the same. Therefore, the relative density of a periodic lattice structure mainly depends on the dimension and strut diameter of the unit cell. Generally, we can enhance the mechanical properties of the given-size lattice structure by increasing the relative density and the number of unit cells.

Most work done on lattice structures are based on normal and simple unit cells. However, some of them shed light on complicated unit cells, whose composition components conform to specific mathematical algorithms, such as gyroid [8, 15, 18, 30, 31], Schwarz diamond [29, 44] called TPMS (triply periodic minimal surfaces), and plate lattices [37]. Compression and tension tests were applied in studying F2CC,Z (face-centered cubic with two diagonal struts in each face and Z-struts), hollow spherical unit cells by Kohnen et al. [13], and concluded that the mechanical properties for F2CC,Z are better than hollow spherical. Contuzzi et al. [45] studied F2CC,Z structure and conducted compressive testing using two samples of different volume fractions and concluded that increasing strut thickness is more significant than introducing other reinforcement struts in the lattice structure. Rehme et al. [11] investigated not only F2CC,Z, but also FCC (face-centered cubic) and F2BCC,Z (body-centered and face-centered cubic combined with Z-struts)

structures. The difference between these three face-centered cubic unit cells can be seen in **Figure 1**(a), (b), (e). BCC (body-centered cubic), BCC,Z (body-centered cubic with Z-struts), gyroid and rhombic were also analyzed through compressive, tensile, and fracture testing [8, 16, 24, 44, 46–48]. They got into a conclusion that F2CC,Z has higher capacity for carrying loads, and gyroid is in requirement for applications needing high stiffness. Peto et al. [49] and Park et al. [17] also extended their interest to other kinds of unit cells, which are relatively uncommon and not widely applied, and finally found that CD (cubic diamond) exhibited higher strength compared to others. Besides, lattice structures/unit cells can also be classified into stretching dominated and bending dominated ones according to their different mechanical properties [41]. Stretching dominated lattice structures undergo tensile or compression stress, while bending dominated lattice structures mainly undergo bending stress, and stretching dominated lattice structures can be much stiffer than bending dominated ones [42]. An image of some unit cells mentioned above is shown in **Figure 1**. All of these are self-supported for 3D printing except FCC and CD structures.

However, the geometrical constraints cannot be ignored for the design of additively manufactured structures. One of the limitations of AM is the overhang angle measured relative to the horizontal plane [50]. Studies show that the geometric discrepancy and surface roughness of the structure will increase as the overhang angle decreases [1, 51–54]. Supplementary supporting structures are necessary to prevent severe distortion or collapse during the AM process if the angle is less than 35° [50]. In this case, self-supporting lattices/unit cells with overhang angles bigger than 35° are applicable for AM.

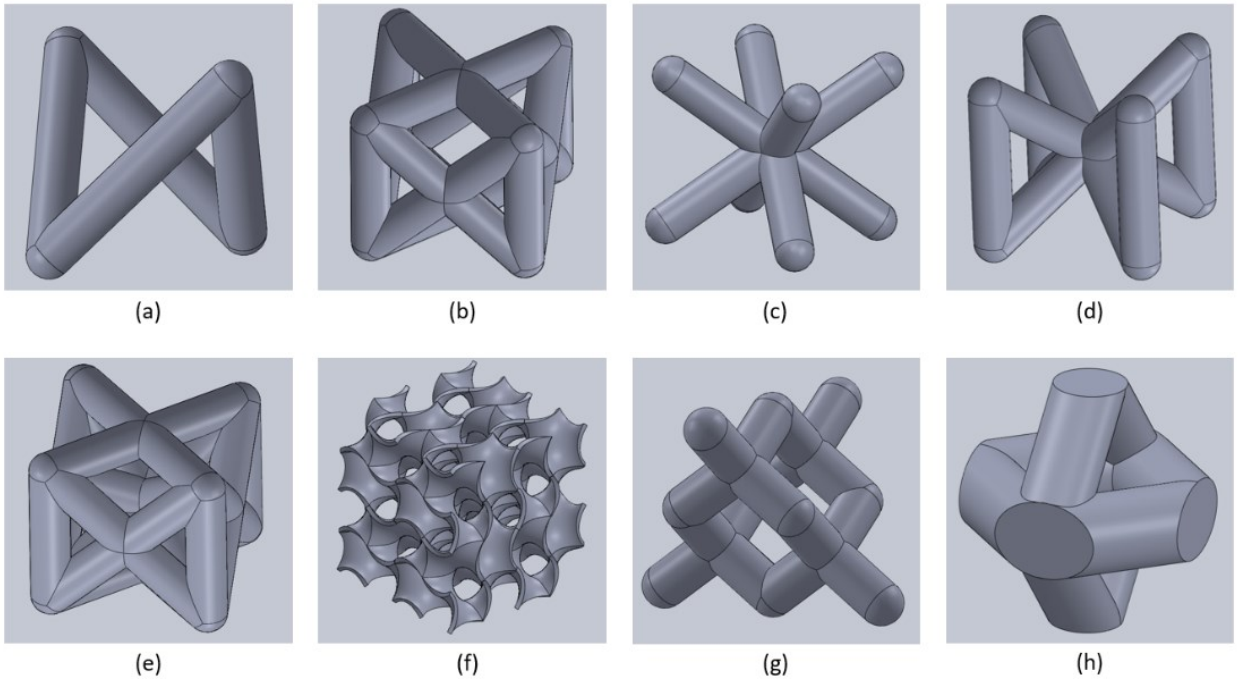

Figure 1. Unit cells in lattice structures: (**a**) FCC; (**b**) F2CC,Z; (**c**) BCC; (**d**) BCC,Z; (**e**) F2BCC,Z; (**f**) gyroid; (**g**) CD; (**h**) Ansys Space-Claim™ diamond.

Among all unit cells, diamond unit cells are considered the best choice for structures with high strength requirements. With predictions of the Gibson-Ashby model, research done by Maconachie et al. [44] manifested that diamond lattice structures exhibit larger relative strength and relative modulus at the same volume fraction of lattice than other lattice structures. However, traditional diamond unit cells, namely CD unit cells, are not self-supported, which might cause some problems in fabrication through AM; hence, another type of diamond unit cell inspired by ANSYS Space-Claim™ is plotted in **Figure 1**(h). This diamond unit cell was shown in the lattice auto-generating feature in the Space-Claim, yet there is limited research literature on its properties. Consequently, this diamond unit cell constructed for the lattice structure was selected in this study because it was anticipated to exhibit higher stiffness than other lattice structures with the same density [55], and it is self-supported which is applicable for AM.

1.3 Bimetallic Composite

A bimetallic composite is a metal matrix composite material composed of two different metal alloys gradually or suddenly transiting from one to another. Bimetallic composites displayed excellent thermal and mechanical properties, as well as high corrosion resistance required by the nuclear, marine, aerospace, and tool industries.

Bimetallic composites were initially manufactured through the welding process, such as laser welding for Cu/steel composite [56], cold-rolled welding for Al/Cu composite [57], and explosion welding for Inconel 625/pain carbon steel composite [58]. Besides, casting is another traditional fabrication method for bimetallic composites. Simple gravity casting and gravity die casting were applied to fabricate aluminum/steel bimetallic composites and Al-Si alloy/cast iron for automotive suspension parts in [59] and [60], respectively. MAM can also be used for bimetallic composite fabrication. Direct energy deposition (DED) is the most common AM technique for this fabrication by transiting the powder feedstock from one metal to another. A variety of studies have gone deeply into this DED technique by researching Ti6Al4V/stainless steel [61, 62], Inconel 625/copper alloy [63], Ni/stainless steel [64], and Cu/steel [65].

Nowadays, SLM is regarded as another MAM technique that owns the capability of manufacturing bimetallic composites due to the limits of DED for its low resolution to be applied to complex structures, even though it is worth noting that transforming the original SLM system to composite manufacturing is much more complicated compared to the DED approach [55]. A multi-material SLM prototype system with two metallic powders mixture (Fe/Al-12Si) is demonstrated by Demir et al. [66], and proving the feasibility of an AM method based on the powder bed fusion for multi-material fabrication. In the work of Tey et al. [67], SLM process was applied to construct multiple-

materials components with a steep material transition from 316L stainless steel to Ti6Al4V, and a technique though introducing an interfacial composite structure was also proposed to enhance multiple materials bonding, which is feasible for metallic combinations in SLM. Besides, 316L stainless steel and Cu alloy multi-material samples were produced using SLM, and a good metallurgical bonding was found at the bond interface by analyzing the interfacial characteristics [68]. Mei et al. [69] manufactured bimetallic composites of 316L stainless steel and Inconel 718 using SLM, despite some cracks and holes at or near the interfaces.

Combining the bimetallic composite with lattice structures, bimetallic lattice composites are gradually gaining interests among researchers. This latticed composite contains two parts, namely the lattice and the matrix, in which another metal matrix material is filled into the gaps of one metal lattice. There is also much research on the microstructure and mechanical properties of bimetallic lattice structures fabricated by SLM, such as CuSn/18Ni300 bimetallic porous structures [70], and A356/316L interpenetrating phase composites [71, 72], in which [72] investigated the mechanical properties of PrintCast composites through finite element analysis (FEA), coupled with digital image correlation (DIC) to capture the deformation and failure processes.

1.4 Defects of Additively Manufactured Parts and X-ray Computed Tomography

Laser powder bed fusion (LPBF) is an advanced technique that is extensively used for the metal additive manufacturing process in aerospace, automobile, defence and biomedical industries, which opens up many exciting opportunities [73–76]. However, extreme and intense thermal conditions are involved in LPBF, although it is a relatively simple manufacturing process [76]; therefore, inevitable defects will occur in the microstructure. Defects include but are not limited to strut waviness and thickness variation, porosity, cracks, surface roughness, residual stress, grain

structures, undesired phase, and undesirable microstructures, leading to high-stress concentrations [2–6, 73, 76–79]. These defects will undermine the strength of the structure and lead to poor mechanical properties; thus, they are supposed to be further examined and minimized [80].

Many researchers have shed light on the geometric defects and mechanical properties of LPBF manufactured parts. Hastie et al. [81] investigated the influence of processing parameters and heat treatment of LPBF techniques on the internal porosity of AlSi10Mg metallic parts. In the work Best et al. [82], processing defects were found using a Zr-based bulk metallic glass (BMG) printed by the LPBF technique with electron microscopy imaging. It turned out that porous processing defects would lead to a loss in tensile strength.

Among many methods of testing and analyzing defects of metallic parts, X-ray computed tomography (XCT) is a non-destructive evaluation and detective method for additively manufactured components with complex internal configurations, remarkably accurate and valuable for porosity analysis and dimensional measurement [83, 84]. Kim et al. [77] employed XCT measurements with tensile tests on LPBF additively manufactured 17-4 stainless steel dog-bone specimens simultaneously to study the effects of internal defects on the mechanical properties. In the work of Ulbricht et al. [78], the spatial defect distribution in a cylindrical specimen was quantified, with the cylinder fully scanned by XCT. Processing parameters, such as scanning speed, scan spacing, laser power and layer thickness, may also affect the detection of the internal porosities of the LPBF metallic parts [81]. Besides, XCT was also applied to manifest the spatial diversification of the defects [85], porous processing defects that ruin the tensile strength [82], the volume, shape or morphology, spatial location, and distribution of the defect [79, 86], the geometrical distortions [2], and sag and dross defects [87]. The XCT results helped to obtain more precise information to further explore the origin of various categories of defects [76], in order to

reduce or even eliminate microstructural defects in the fabrication process [88].

In addition, high-speed X-ray imaging is another unique tool for investigating defects in additively manufactured metal components to help address building reliability related issues [75]. In situ process monitoring is usually applied along with high-speed X-ray imaging to detect internal defects, predict part properties, and feature local behavior [80]. Guo et al. [89] took insight into the dynamics of powder spattering, which is considered as a vital cause of defects observed with in-situ high-speed X-ray imaging in the LPBF process. High-speed X-ray imaging was also employed by Zhao et al. [90] to monitor the in situ LPBF process, and the same technique was carried out by Bobel et al. [91] as well to indicate the primary source of internal pores. Moreover, X-ray imaging technique with in-situ process monitoring was also employed to measure the dynamic structure parameters in LPBF process [73, 76, 88] and observe the crack formation in the substrate [92].

1.5 Objectives and Scope of the Research

This study was inspired by the accumulated work on lightweight lattice structures and AM. Metallic lattice structures meet the demand for structures with high strength and light weight, and AM is the most widely adopted technique for the fabrication of lattices with complicated internal structures. Literature reviews for additive manufacturing (AM), unit cells of lattice structures, and bimetallic composite enlightened on the research work such as analyzing methodology, approaches of strength validation, and procedures of experiment conduction, as many academics have elucidated.

To maintain the characteristic of the lattice structure, the volume fraction is not supposed to be too large to differentiate from the solid. Thus, we need to balance the volume fraction and the

mechanical strength of the lattice based on the fact that the strength will decrease as the volume fraction drops. Nevertheless, there is still a considerable gap between the strength of the lattice and solid structures; therefore, a novel bimetallic composite is worth being explored, whose strength is enhanced by filling into another metal alloy in lattice cavities, and accordingly, the mechanical properties will be improved without changing the volume fraction of the lattice structure.

However, considering the limitation of AM on the choice of unit cells, we need to be careful with the selection of the unit cell as well. According to the literature, there are still a bunch of self-supported unit cells which meet the prerequisite of AM but were not frequently studied by many researchers. Besides, the defects in structural geometry attributed to the high temperature during AM procedures need to be further explored. Hence, this thesis aims to investigate the mechanical behaviour of novel bimetallic composite lattice with self-supported unit cells compared to bulk/solid structures and further analyze the porosity and geometric deviation of the additively manufactured lattice structures.

Five research questions were proposed before starting the study, and then they were addressed consequently in the following chapters:

1. Which lattice structures offer best specific strength and stiffness?

2. What are the design specifications of AM for the targeted lattice structures?

3. How to build finite element models to simulate the mechanical behaviour of additively manufactured single-metal lattice structures and validate the results experimentally?

4. How to build finite element models to simulate the mechanical behaviour of additively manufactured bimetallic lattice structures and validate the results experimentally?

5. Are there any discrepancies of geometries between AM printed samples and nominal samples generated by SolidWorks™?

Four chapters following the Introduction are organized to address these questions as showed in the flowchart shown in **Figure 2**.

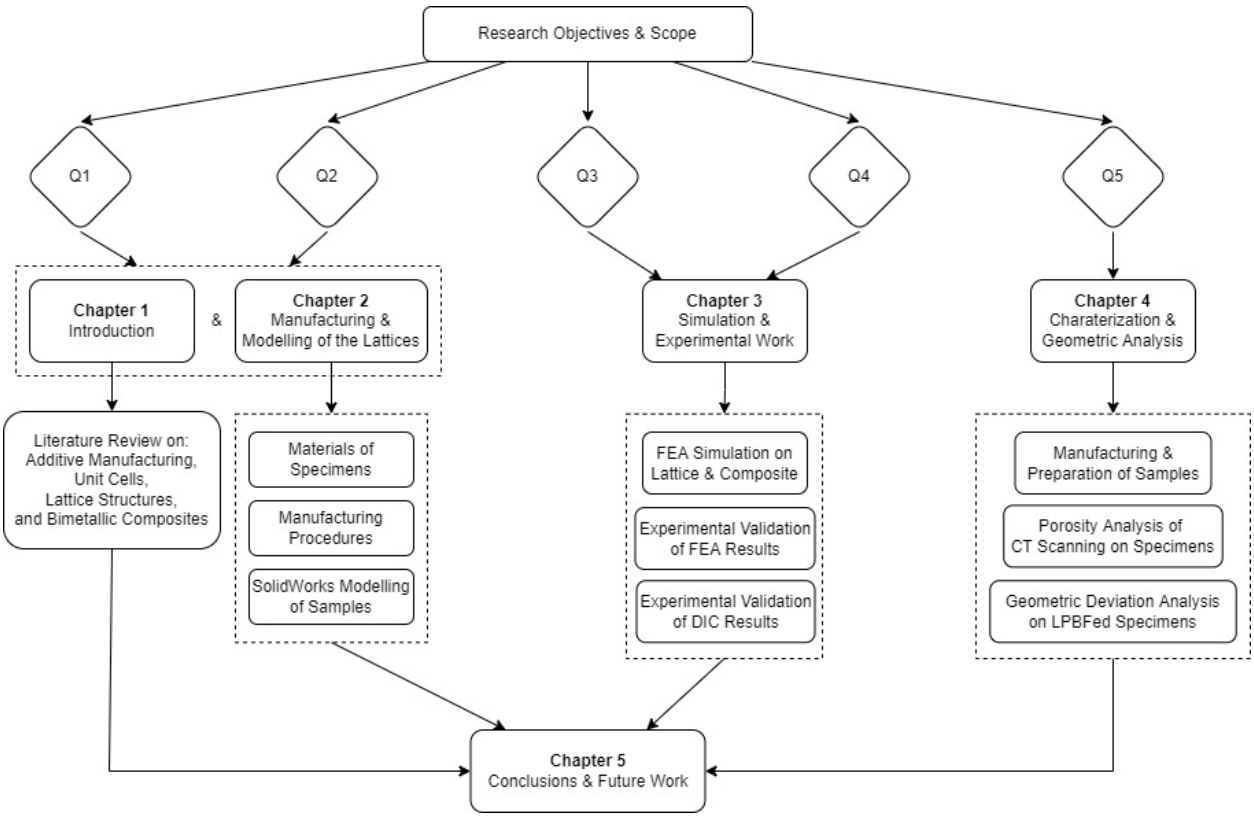

Figure 2. Flowchart of thesis organization.

CHAPTER 2

MANUFACTURING AND MODELLING OF COMPRESSION, TENSION BEHAVIOUR OF MONOLITHIC AND COMPOSITE LATTICE SPECIMENS

2.1 Introduction

To study the mechanical properties of materials and structures, both compression and tension tests were performed. Hence, bulk samples, lattice samples and bimetallic composite samples were required for both tension and compression tests. This chapter introduced the materials 316L stainless steel and dissolvable aluminum alloy for printing the samples. Chemical composition, size of the metal powder as the feedstock of the SLM process, and the manufacturing procedures for both SLM and casting were included. Additionally, computer-aided design models of the samples were also illustrated and presented in figures at the end of the chapter.

2.2 Materials

The argon-atomized 316L stainless steel powder with a particle size range of 15–45 μm was fed for the SLM process. The chemical composition of the 316L stainless steel powder is listed in **Table 1**, while the chemical composition of the aluminum alloy used for the casting process is listed in **Table 2**.

316L stainless steel is one of the most extensively studied materials for additive manufacturing

(AM) credited to its excellent ductility, strength, and corrosion resistance. It has been widely applied in biomedical, marine, chemical, nuclear reactor, and petrochemical industries [93]. The chemical composition of the aluminum alloy used for the casting process is listed in Table 2. This aluminum alloy has been widely utilized in dissolvable oil and gas tool applications and developed fundamentally for mechanical properties of quick-dissolving in a saline-rich environment and high corrosion rate. The corrosion rate is accelerated by the components of Ag and Ga inside, whereas Mg and Cu enhance the strength of the aluminum alloy [55].

Table 1. Chemical composition of 316L stainless steel powder used as the feedstock material for the AM process (wt.%).

Chemical Composition	C	Cr	Mn	Mo	N	Ni	O	S	Si	Fe
Value (wt.%)	0.03	17.9	2.0	2.4	0.1	13.9	0.04	0.01	0.75	Balance

Table 2. The chemical composition of the aluminum alloy used for casting (wt.%).

Chemical Composition	Fe	Ag	Ga	Cu	Mg	Al
Value (wt.%)	0.6	2.1	2.0	2.6	4.1	Balance

2.3 Manufacturing

Stainless steel 316L lattice samples were printed through an EOS M290 machine (EOS, Krailling, Germany), equipped with a Yb-fiber laser, while a proprietary aluminum alloy supplied by the industrial partner (PRECISION ADM) was used for the filled-in matrix part of composite by casting. Bulk aluminum samples were also fabricated by casting to better explain the microstructure and mechanical behavior of the bimetallic composites.

The compression and tension lattice structures were manufactured by selective laser melting (SLM). The tensile specimens were fabricated in a horizontal orientation with respect to the build

plate, which was a hot-rolled mild steel panel with dimensions of 252 mm × 252 mm × 25 mm. The processing parameters of layer thickness, scan speed, laser power, and hatch spacing recommended by EOS Company have been employed as 20 μm, 1083 mm/s, 195 W, and 80 μm, respectively. An alternating scan pattern was applied to all the lattice parts, and the hatching direction of each layer was rotated by 67°. Additionally, super-pure argon gas was purged into the building chamber to maintain an oxygen level of less than 0.1% during the printing process. The build plate temperature was kept at 80 °C to reduce stresses imposed by thermal cycles.

As of the casting process, there is a wax shell with a 2 mm thickness covering the SLM fabricated stainless steel lattices. The wax shell on the lattice prevented the penetration of the slurry into the lattice cavities. The plaster mould was made by a commercial investment powder (Plasticast BANDUST) mixed with water under the powder/water weight ratio of 0.4. The slurry was then poured into a flask containing the stainless steel lattices. To guarantee that the flask was filled adequately with slurry, it was exposed to a vacuum (10^{-5} Pa) for 90 s. It was then heated up to 732 °C to dissipate the wax after slurry hardening at room temperature, followed by the mould dehydration and residual carbon elimination by furnace cooling to room temperature. The plaster mould containing the stainless steel lattices was preheated to 250 °C and held for an hour in an oven. The aluminum alloy feedstock was placed in a graphite crucible, heated up to 850 °C and held for 1 h in an electrical furnace. The mould containing the stainless steel lattices was placed on a vacuum table after the heating was done. Subsequently, the superheat molten aluminum alloy with a temperature of 850 °C, which is used to enhance the fluidity of the molten aluminum, was immediately poured into the plaster mould and infiltrated the 316L stainless steel lattice cavities under the vacuum to yield the bimetallic composite parts. Bulk aluminum parts without stainless steel were also cast under the same conditions.

An image of all experimental samples in this study is illustrated in **Figure 3**, and each type was printed for 3 duplicates for repeated tests.

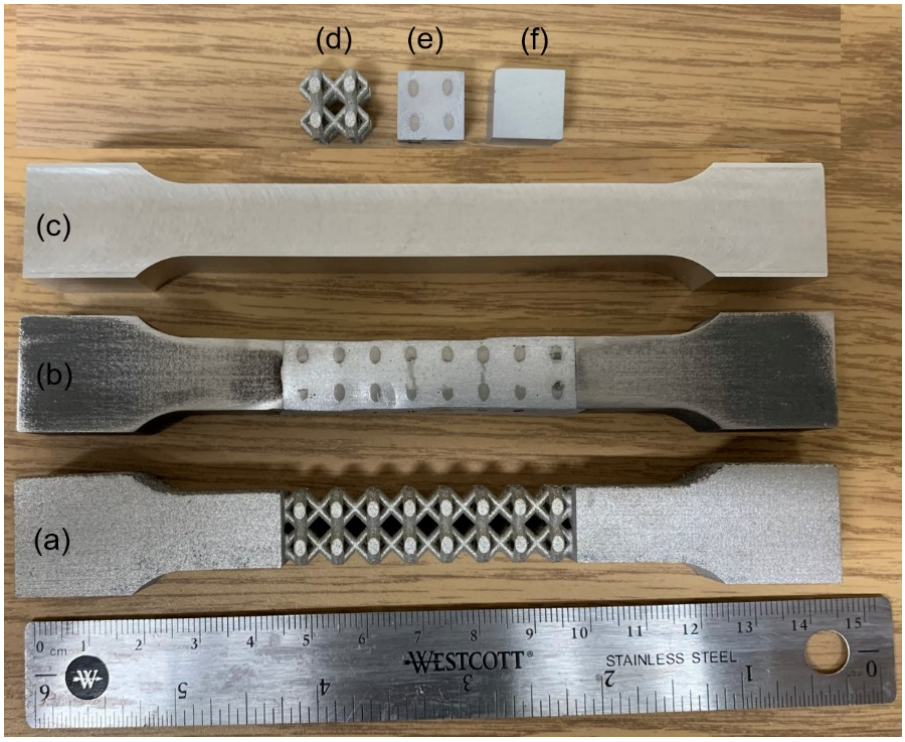

Figure 3. An image of the experimental samples: (**a**) stainless steel lattice dog-bone; (**b**) stainless steel/aluminum composite dog-bone; (**c**) bulk aluminum dog-bone; (**d**) stainless steel lattice cube; (**e**) stainless steel/aluminum composite cube; (**f**) bulk aluminum cube.

2.4 SolidWorks Modelling

All nominal models with either lattice structures or bulk parts were made by SolidWorks™. A cube geometry was selected for compression specimens, while tension samples' design had to refer to the ASTM standard, which is a shape of the dog bone. As for composites, the cavity portion was formed by subtracting the lattice from a complete cube or dog bone; then, the composite was created by assembling the lattice part with the cavity portion.

Figure 4 and **Figure 5** show the computer-aided design (CAD) models of compression and tension samples for lattice, bulk and composites.

2.4.1 Compression Specimens

Lattice compression samples were in the shape of a cube with a height of 12.5 mm. The diamond unit cell was chosen for the lattice structure, with a strut diameter of 2 mm. The length, width, and height of the unit cell are equally to be 6.25 mm; hence, in order to form a 12.5 mm cube model, the linear pattern was applied with the amount of two unit cells in each direction. Therefore, the compression lattice model was created by stacking 8 unit cells together shown in Figure 4(c).

The compression bulk model shown in Figure 4(d) was a simple cube with a height of 12.5 mm extruding from a 12.5 mm × 12.5 mm square through SolidWorks™.

2.4.2 Tension Specimens

The tension samples of lattice shown in Figure 4(a) were a dog-bone shape, whose dimensions conformed to ASTM E8M standard [94], with a gauge length of 50 mm, a gauge width of 12.5 mm, and an overall length of 140 mm. The lattice structure unit cell's strut diameter is 2 mm, which is the same as compression lattice samples. Failure of the tension samples should occur in the gauge zone rather than the interface between the diamond lattice part and the solid gripping part, which is the location of stress concentration. Therefore, fillets were designed on the junction interface of grips to reduce the concentrated stress and avoid failure in this area. The 0.75 mm fillets of the tension sample and the compression sample are displayed in Figure 4(e).

The tension bulk model was a simple dog bone with the same length shown in Figure 4(b), height and width as the lattice one, and the gauge length part was fulfilled with the solid structure instead of the linear-patterned lattice.

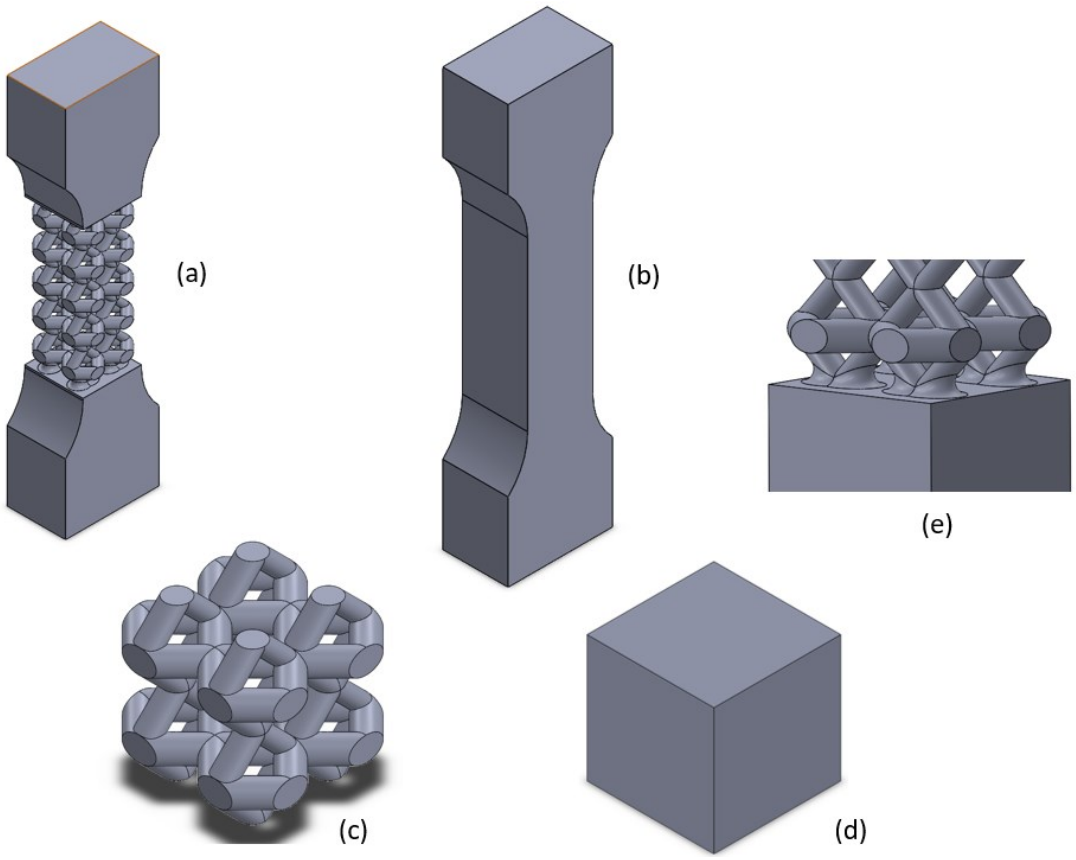

Figure 4. Computer-aided design models (CAD) of the Space-Claim diamond lattice structure parts: (**a**) tension lattice dog-bone model; (**b**) tension bulk dog-bone model; (**c**) compression lattice model; (**d**) compression bulk model; (**e**) fillets in the interface of tension dog-bone model.

2.4.3 Composite Specimens

Bimetallic composite samples were manufactured based on the lattice ones. Firstly, the cavity/matrix portion needed to be created by subtracting the lattice part from its base bulk model. Separate models of both compression composite and tension composite created in SolidWorks™ are shown in **Figure 5**. Then, the composite will be made by assembling the lattice part with the matrix portion, simply mating their part mass-centers together.

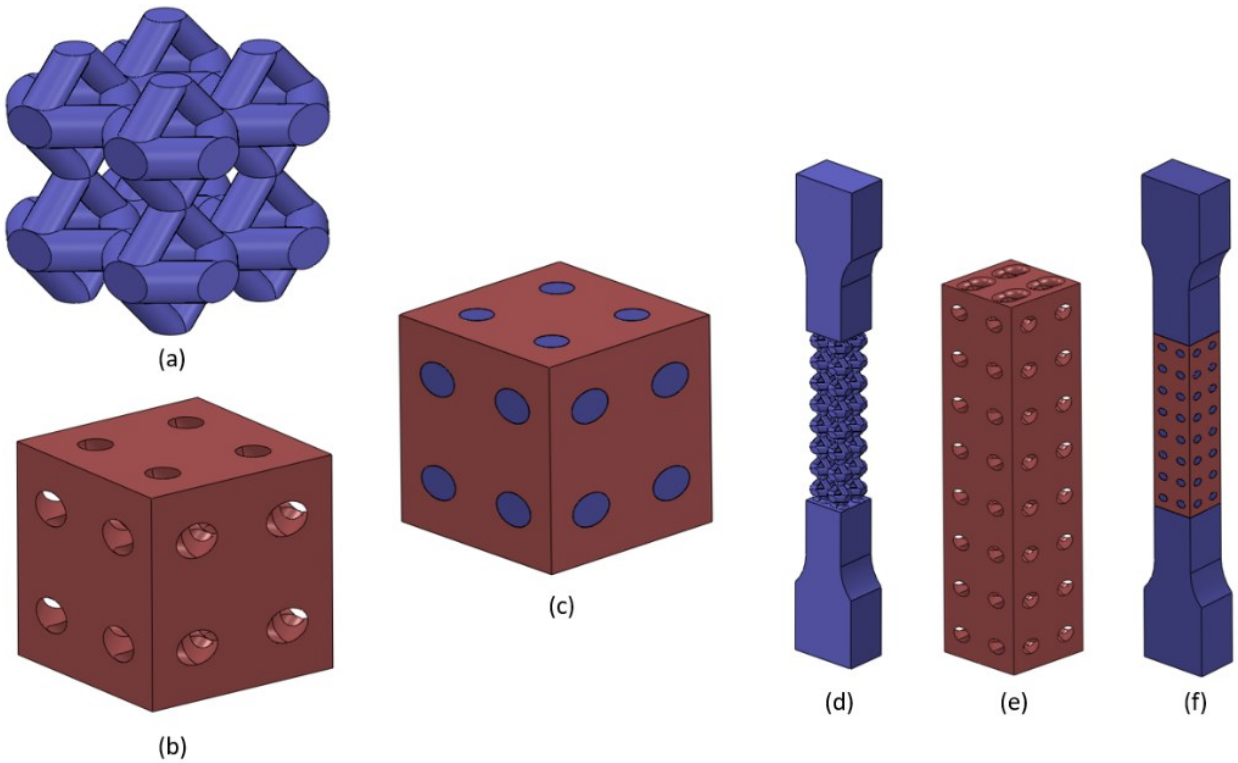

Figure 5. CAD models of the composite parts: (**a**) lattice part for the compression composite; (**b**) matrix part for the compression composite; (**c**) the compression composite; (**d**) lattice part for the tension composite; (**e**) matrix part for the tension composite; (**f**) the tension composite.

CHAPTER 3

SIMULATION AND EXPERIMENTAL WORK ON UNIAXIAL BEHAVIOUR OF BIMETALLIC LATTICE COMPOSITES

3.1 Introduction

Finite Element Analysis (FEA) is commonly used for simulating the experimental process and validating testing results. Researchers usually conducted FEA for performance evaluation [94–96], structure design [97], investigating configurational effects [98], and studying the failure mechanism [99, 100]. Besides, digital image correlation (DIC), which is applicable for 3D and full field measuring of deformation and strain on almost any material without contacting, is also essential for investigating strain rate by analyzing captured images, and it is also clear to point out elongation changing along side the experiments processing. Limited research was done for analyzing deformation and strain evolution applying DIC on stainless steel such as 316L [13, 72, 101]. Mostly, the focus has been on studying titanium alloy Ti6Al4V [102–105]. Other investigations into displacement, velocities, and stress measurements using DIC were also done on polymers [106], glass fibers [107], and other materials [108, 109].

This chapter introduces the finite element model (FEM), which can be applied to the single material and bimetallic additively manufactured lattice structures through ABAQUS™. Lattice and bulk specimens are discussed apart from the bimetallic composite samples. Digital image correlation (DIC) system is further mentioned for the function of image capturing along with the experimental process. The validation between FEA and DIC data and experimental results is also

clarified by comparing the discrepancies of the final curve plots.

3.2 Simulation

The FE analysis was conducted using the commercial FE code ABAQUS™/Explicit (2019 version, Dassault Systemes, Vélizy-Villacoublay, France) [110], with simulation models generated using SolidWorks™. Comparing to ABAQUS™/Standard, ABAQUS™/Explicit solver can solve the convergent problems for models with complicated internal structures in a better way, especially for lattice structures. Furthermore, it can also readily analyze contact interaction problems between the independent bodies [72] for the bimetallic lattice structures.

The simulation model needs to be imported into ABAQUS™ before conducting the FE analysis. Then, the material parameters such as Young's modulus, Poisson's ratio for elasticity, and "true stress" vs. "plastic strain" values for plasticity in the ABAQUS™ property-material module are set up. The plasticity "true stress" vs. "plastic strain" pairs of values for 316L stainless steel were obtained from [111], while data for aluminum alloy were obtained from the bulk aluminum experiments. After setting up the properties of materials, assigning the specific material to the specific part accordingly, for example, 316L stainless steel was given to the lattice parts while aluminum was given to the bulk aluminum parts.

3.2.1 FEA of Lattice and Bulk Specimens

The plasto-elastic model was selected in ABAQUS for FEA simulation. For compression model boundary conditions, the bottom end (one surface for bulk models, four small surfaces for lattice models) was fixed for all the six degrees of freedom (U1 = U2 = U3 = UR1 = UR2 = UR3 = 0). The bottom end was totally fixed because there was no notable difference on the end surface before and after the shape deformation of the experimental tests, which will be validated later by the DIC

results in the Section 3.3.3.1. Simultaneously, a reference point was generated on the top and coupled with the top end (one surface for bulk models, four small surfaces for lattice models), with five degrees of freedom fixed (U1 = U3 = UR1 = UR2 = UR3 = 0) and one remained (U2) for the loading. A velocity of 0.5 mm/min was then applied to the top reference point in the U2 direction. Note that the applying velocity should not be consistent from the beginning of the analysis until the end. Based on the actual experiment, the loading speed shall change gradually from 0 mm/min initially, to the maximum in the middle, then drop back to 0 mm/min in the end, at which time the average rate would be 0.5 mm/min. In this case, the amplitude of velocity gradually changed throughout the whole loading process. As for tension models, similarly, the bottom end of the dog-bone gripping area was fixed for all degrees of freedom (U1 = U2 = U3 = UR1 = UR2 = UR3 = 0), while a velocity of 2 mm/min was applied to the reference point on the top in the U2 direction (U1 = U3 = UR1 = UR2 = UR3 = 0).

The last step before running the FE analysis was meshing. The free linear tetrahedral 3D stress element (C3D4 element type) was selected for both compression and tension lattice models and tension bulk dog bones, while the structured linear hexahedral 3D stress element (C3D8 element type) without reduced integration was used for compression bulk samples. Note that C3D4 was also used on the gripping block areas of tension lattice models to assure consistency with the lattice part. It turned out that after studying the mesh sensitivity, the mesh was stable between the mesh size of 0.5 mm and 2 mm. To maintain the FEA simulation accuracy and decrease the simulation time to a certain degree, the mesh size chosen for compression lattice samples is 0.5 mm, and 1 mm for all other models. The 5% trivial deviation of the FEA results shown in **Figure 6**, with mesh size 0.5 mm and 1 mm for the 316L lattice, indicates the feasibility of applying a mesh size of 1 mm. For the compression bulk 316L stainless steel model, the compression bulk aluminum

alloy model, and the 316L stainless steel lattice model, the numbers of elements are 2197, 2197 and 47,336, respectively, with node numbers of 2744, 2744, and 10,895. For the tension bulk 316L stainless steel model, tension bulk aluminum model, and tension 316L stainless steel lattice model, the numbers of elements are 158,001, 158,001, and 188,681, respectively, with nodes numbers of 30,622, 30,622, and 40,588.

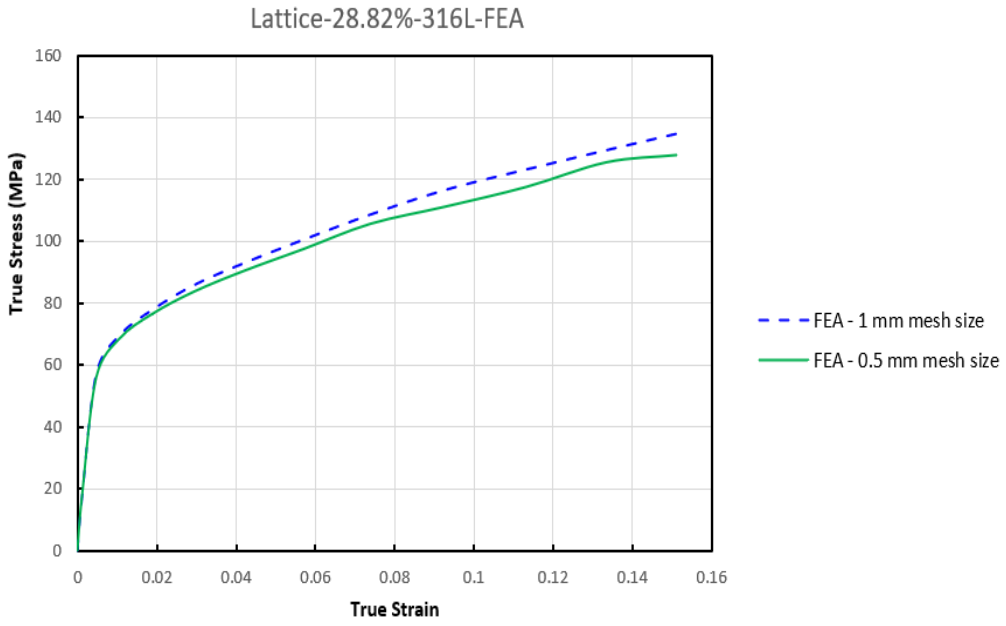

Figure 6. Comparison of mesh sensitivity between the sizes of 0.5 mm and 1 mm of 316L lattice.

Figure 7 and **Figure 8** show deformation contour plots for bulk 316L stainless steel, bulk aluminum, and 316L stainless steel lattice under both compressive and tensile conditions. Stresses shown in the plots were all von Mises stress averaging at 75%. The value 75% here means if the relative discrepancy between the contributions that a selected node gets from its neighboring elements is a smaller amount than 75%, these contributing values are averaged [110]. The local effects on **Figure 7**(a), (b) might come from the contact boundary condition applied. The rigid

plate is used to apply the compressive load to the sample. When the deformation reaches the highest level in compression, friction between the rigid surface and the sample surface will lead to "sticking condition" which leads to much higher result as seen in the model results. This however only accounts for a very limited range of the whole load carrying area. As a result, the actual stress used to represent the bulk behavior of the compression sample is much less than the 1110 MPa as shown. The same situation applies to the **Figure 7**(b). It is also evident that 316L stainless steel is much stronger and can afford more stress than aluminum under both compressive and tensile conditions. Moreover, compressive strength is almost the same as tensile strength for the lattice sample since there is no significant difference between their ultimate stress in the deformed contour plots.

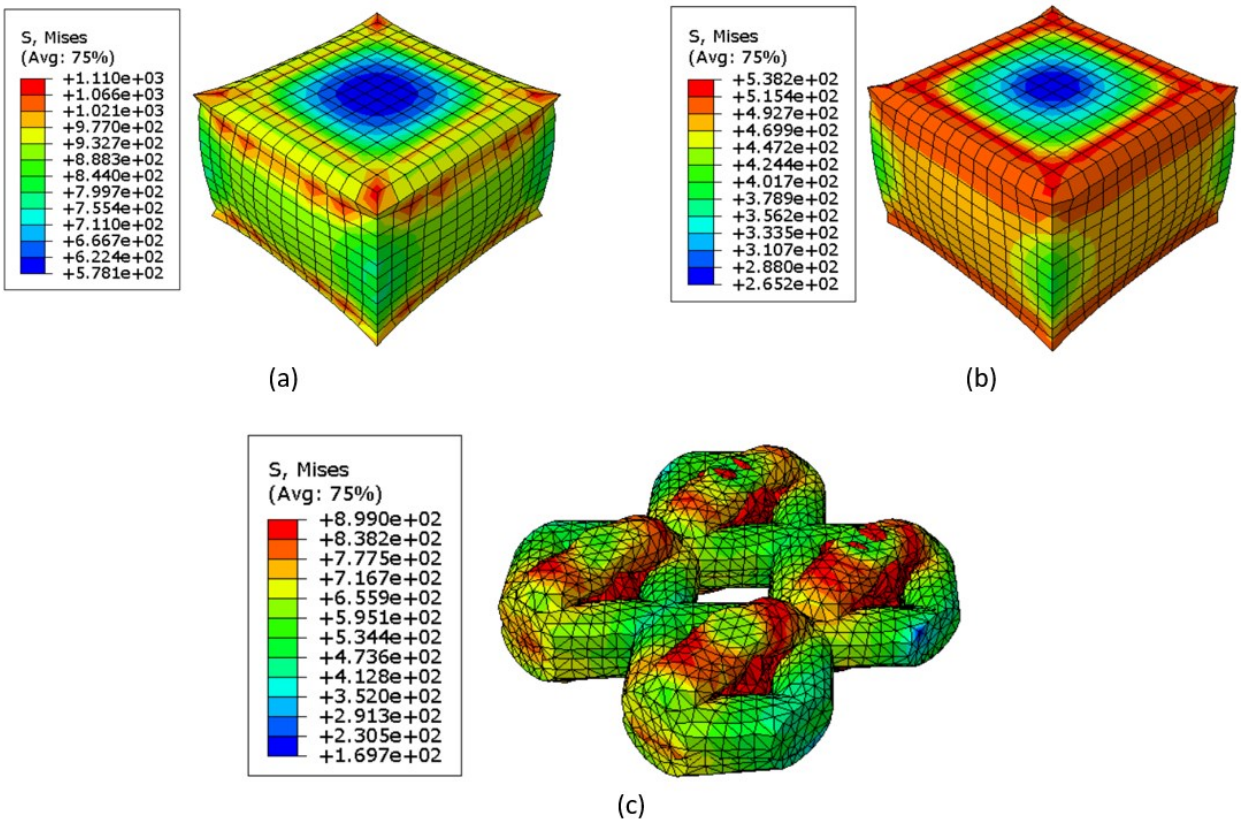

Figure 7. Deformation contour plots of FEA for compression samples: (**a**) bulk 316L stainless steel cube; (**b**) bulk dissolvable aluminum cube; (**c**) 316L stainless steel lattice.

After getting the contour plot, the reaction force and displacement of the top reference point of each model were exported from ABAQUS™ to an excel sheet. The engineering stress (σ_E) and engineering strain (ε_E) were obtained using the equations below:

$$\sigma_E = \frac{The\ reaction\ force\ (N)}{The\ failure\ cross\ section\ area\ (mm^2)}, (MPa) \quad (1)$$

$$\varepsilon_E = \frac{The\ displacement\ (mm)}{The\ sample\ (gauge)\ length} \quad (2)$$

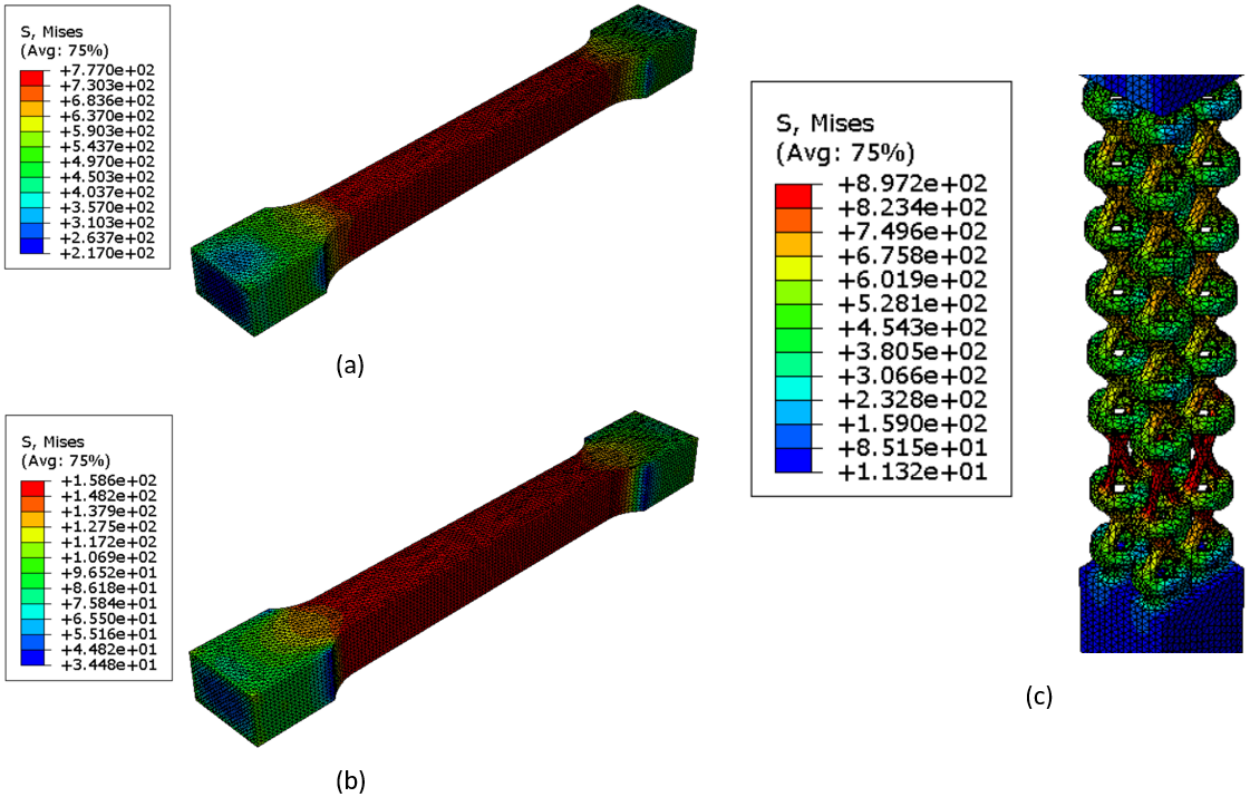

Figure 8. Deformation contour plots of FEA for tension samples: (**a**) bulk 316L stainless steel dog-bone; (**b**) bulk dissolvable aluminum dog-bone; (**c**) 316L stainless steel lattice dog-bone.

The compression model is a cube of 12.5 mm in each direction, and the gauge length for all tension models is 50 mm. The cross-section area for both compression and tension bulk models is 156.25 mm^2 (12.5 mm × 12.5 mm). However, as the cross-section area varies throughout the whole length

of lattice samples, the average cross-section area size of 60.99 mm^2 is adopted with a maximum of 109.42 mm^2 and a minimum of 12.56 mm^2. **Figure 9** shows the positions of maximum and minimum areas of the lattice using the compression one as the example.

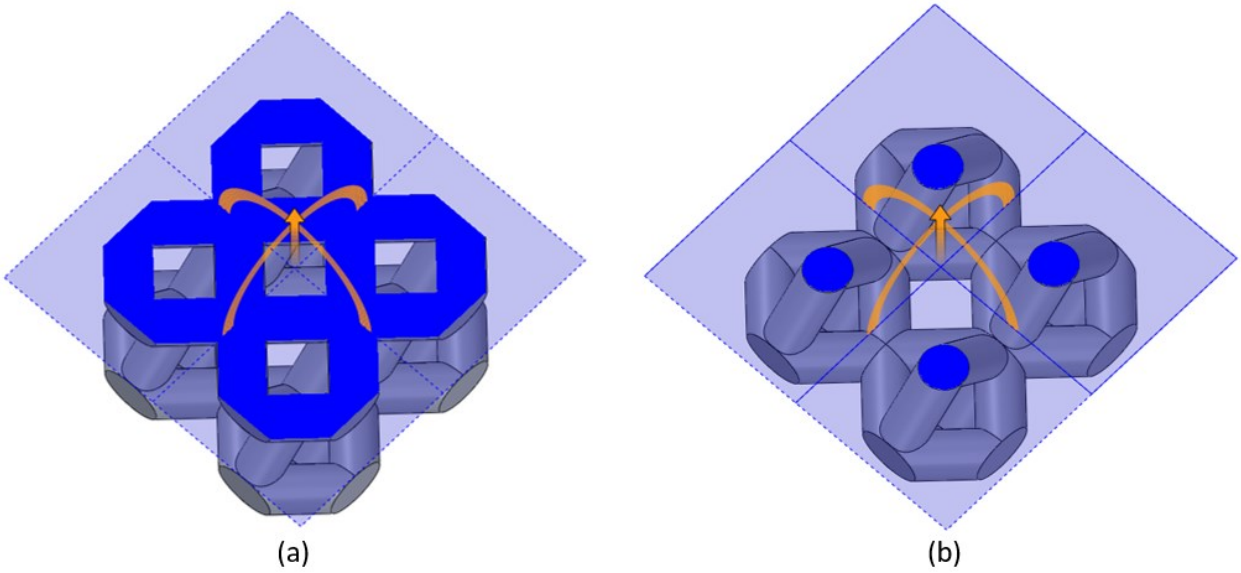

Figure 9. Maximum and minimum areas of the compression lattice model: (**a**) maximum area and (**b**) minimum area.

Using the formulas below, we can convert the engineering stress (σ_E) and engineering strain (ε_E) to true stress (σ_T) and true strain (ε_T):

$$\varepsilon_T = \ln(1 + \varepsilon_E) \tag{3}$$

$$\sigma_T = \sigma_E(1 + \varepsilon_E) \tag{4}$$

The "true stress" vs. "true strain" plots for FE compression and tension tests are shown in **Figure 10** and **Figure 11** below. The experimental work will be discussed in Section 3.3.3.1, and the comparison will be made between the FEA and experimental results to verify the consistency.

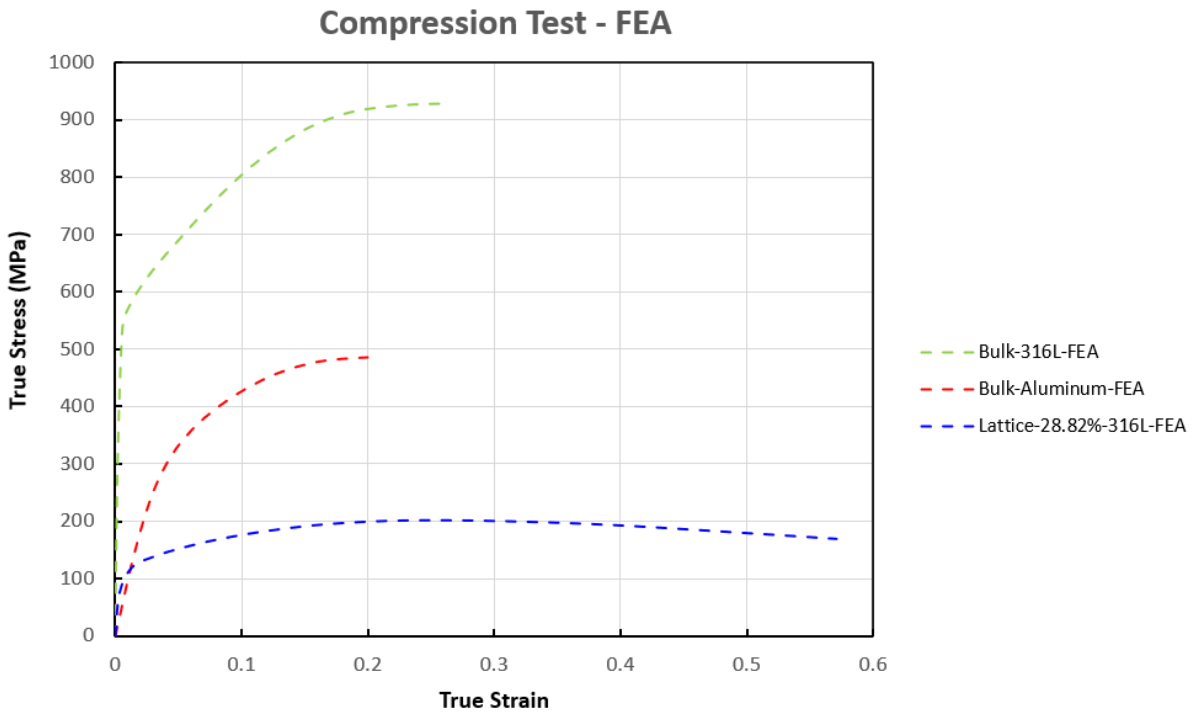

Figure 10. FEA results of bulk 316L stainless steel, bulk dissolvable aluminum, and 316L stainless steel lattice for the compression test.

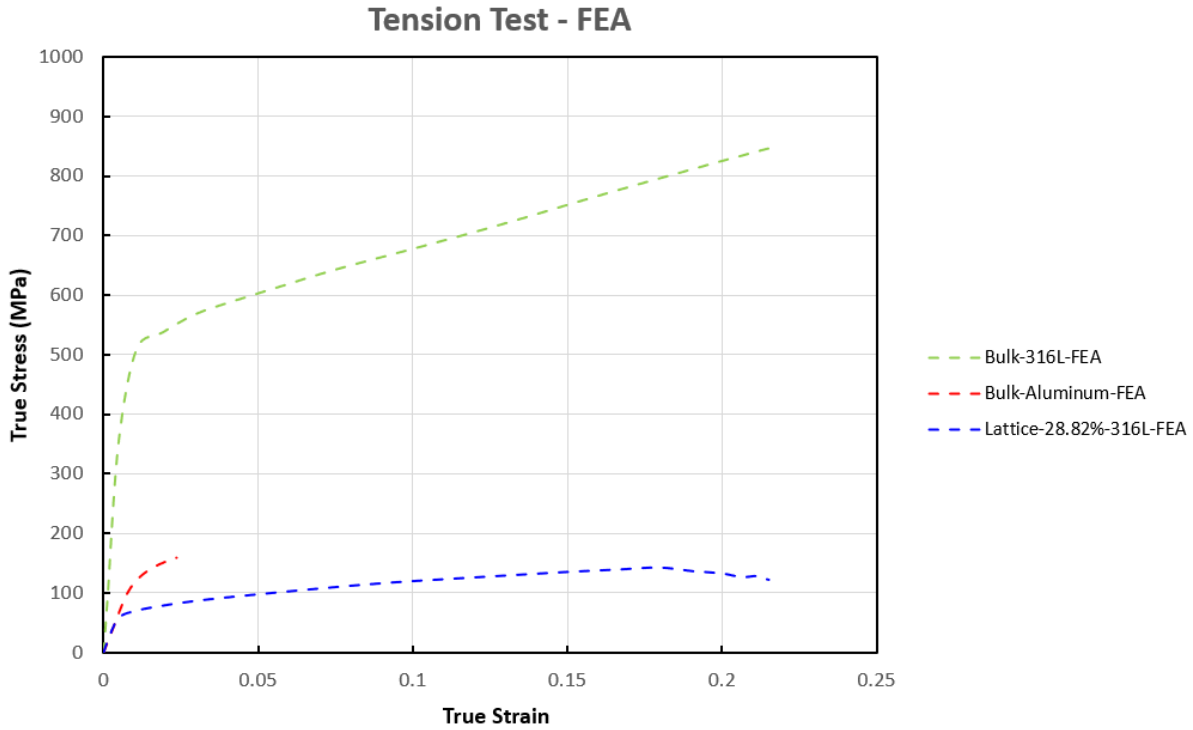

Figure 11. FEA results of bulk 316L stainless steel, bulk dissolvable aluminum, and 316L stainless steel lattice for the tension test.

3.2.2 FEA of Bimetallic Composite Specimens

For FEA modeling of the bimetallic composite, two separate models were constructed in SolidWorks™ and imported and combined in ABAQUS™. ABAQUS™/Explicit (2019 version) solver was used in this work as it is appropriate to solve problems involving two models contacting each other. The plasto-elastic model was selected in ABAQUS for FEA simulation.

Similar to the procedure in Section 3.2.1, the materials were assigned to the corresponding part of the composite after importing the models into ABAQUS™. Materials for both compression composite and tension composite are the same, namely 316L stainless steel for the lattice part, and aluminum for the filled-in matrix part. Next, separate models were assembled into one composite pattern, and the geometry centers of both the lattice part and the matrix part were ensured to coincide. Setting up interaction between two objects of a composite is critical in ABAQUS™ FEA. Based on the microstructural analysis of the interface as reported in [55], it is observed that there is no cohesive bonding between the two parts, and therefore, a “hard contact” interaction of the 316L/aluminum interface was generated in ABAQUS™. Two surface sets were established, with one set of the outer surfaces of the lattice, and the other of the inner surfaces of the matrix, to be selected for creating the surface interaction. No penetration in the normal direction is assumed, and isotropic friction with a coefficient of 0.3 in the tangential direction is applied without elastic slip and any other shear stress for both the compression and tension composite patterns. Finally, a reference point is created on the top surface and coupled with the top cover for applying the load.

The boundary conditions for both compression and tension composites are the same as the models for bulk and lattice experiments. The bottom end was fixed for all the six degrees of freedom (U1 = U2 = U3 = UR1 = UR2 = UR3 = 0), and the top reference point was held for five degrees of

freedom except for U2 (U1 = U3 = UR1 = UR2 = UR3 = 0). A gradually changed velocity of an average of 0.5 mm/min was applied on the reference point for the compression sample, while 2 mm/min for the tension, maintaining consistency with the experiments. Figures of boundary conditions for compression and tension composites are omitted here since there is no significant difference with those shown in Section 3.2.1.

The free linear tetrahedral 3D stress element (C3D4 element type) was applied to both the lattice and matrix part of compression and tension composites. It is worth noting that the gripping block areas of the tension composite dog-bone also used C3D4, which is identical to the tension lattice dog-bone meshing. The mesh was stable between the mesh size of 0.5 mm and 2 mm from the mesh sensitivity study. To give a good bounce of accuracy and efficiency, the mesh size for the compression composite was 0.5 and 1 mm for the tension composite. Moreover, there are overall 152,845 and 327,547 elements, and 32,891, and 70,978 nodes for the whole compression and tension composites, respectively.

Figure 12 gives the deformation contour plots of two composites. Stresses shown in the plots were all von Mises stress averaging at 75% of elongation. We can see that the composite is severely deformed under the compressive loading, and the matrix part is in light-green color, which means it afforded the load and played an essential role in resisting the load. In contrast, the tension composite matrix is almost in the blue color. Compared with the scale bar, we know that the insignificant load transferred to the matrix. This is due to a lack of interface fusion due to continuous cracks in the 316L/aluminum interface preventing the load transfer from the lattice to the matrix.

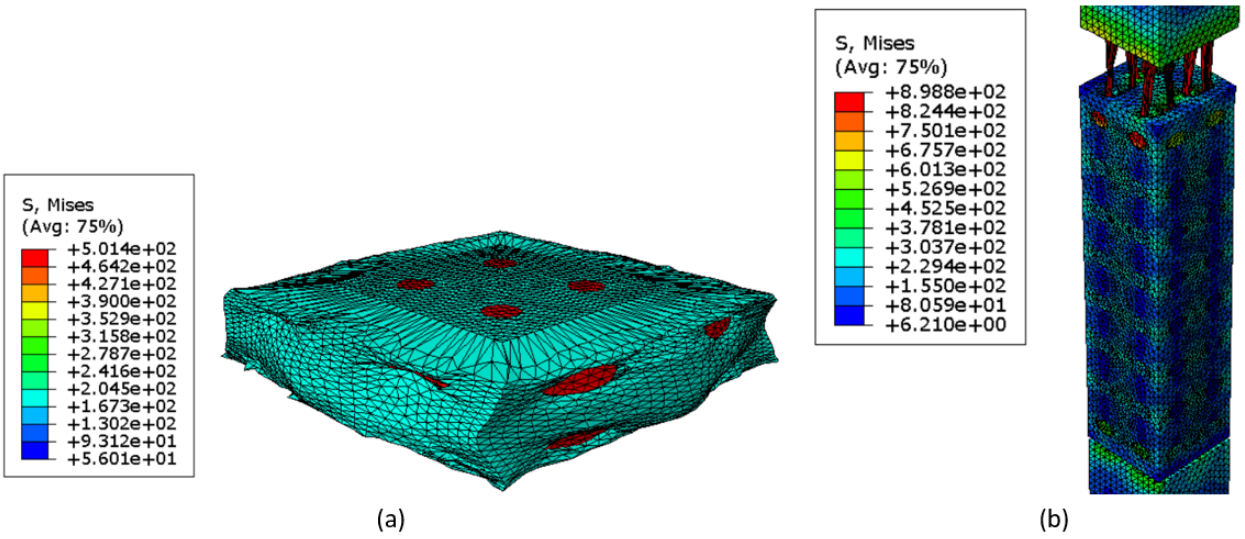

Figure 12. Deformation contour plots of FEA for composite samples: (**a**) compression composite cube and (**b**) tension composite dog-bone.

"Engineering stress" and "engineering strain" were then collected from the reaction force and displacement exported from ABAQUS™ using Equations (1) and (2), and corresponding "true stress" and "true strain" were calculated by Equations (3) and (4). The sample length was 12.5 mm for the compression composite, while 50 mm (gauge length) for the tension composite. The cross-section area was 156.25 mm^2 (12.5 mm × 12.5 mm) for the compression; however, this is not the case for the tension.

The "true stress" vs. "true strain" plots for compression and tension composite FEA results are shown as dashed black lines in **Figure 13** and **Figure 14**, respectively, and overlapped in Section 3.3.3.2 for comparison. Similarly, the experimental work will also be discussed, and the comparison will be made between the FEA and experimental results to verify the consistency.

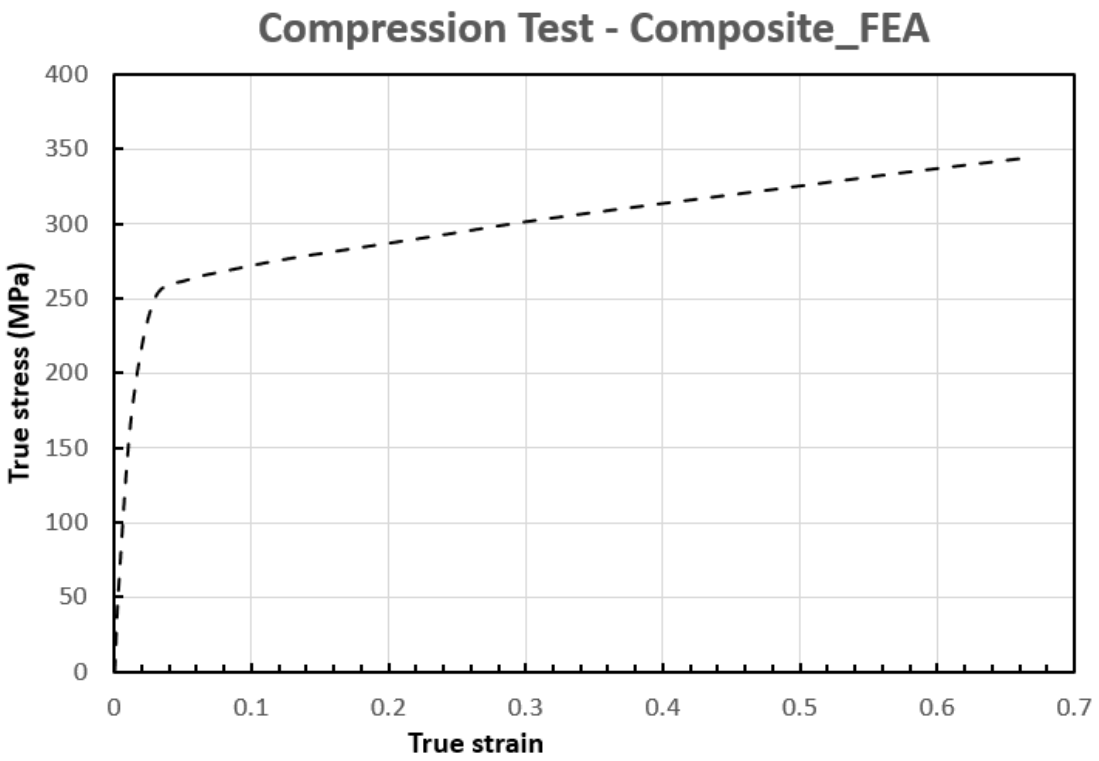

Figure 13. FEA result of the compression composite in the compression test.

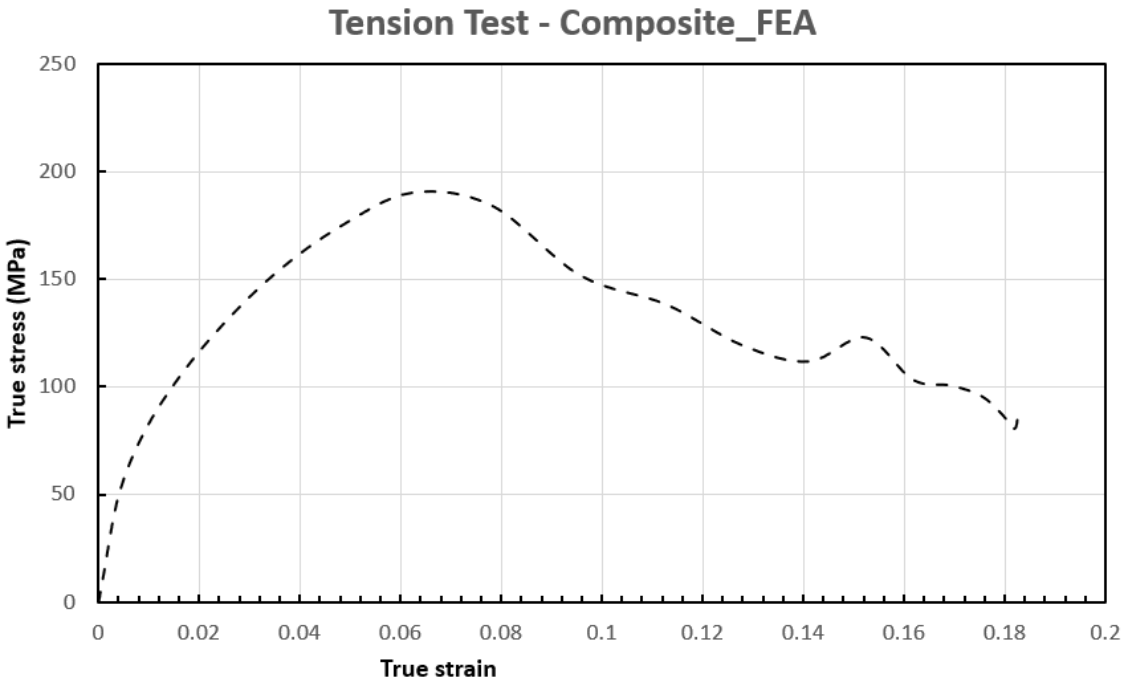

Figure 14. FEA result of the tension composite in the tension test.

3.3 Experiments

Unexpected defects of additively manufactured samples are not avoidable, such as microporosity and strut waviness. Therefore, it is necessary to proceed with the experimental work on uniaxial behaviour and examine the strength of the manufactured structure. Experiments were on the MTS 810 machine, while DIC equipment was capturing experimental images for strain analysis.

3.3.1 Digital Image Correlation (DIC) System Setting

In our experiments, VIC-Snap commercial software (V8, manufactured by Correlated Solutions, Inc., Irmo, SC, USA) was used to capture images, and VIC-3D commercial software (V8, manufactured by Correlated Solutions, Inc., Irmo, SC, USA) was applied to process the images.

Two Allied Vision Technology (AVT) Pike F421b cameras (resolution of 2048 (H) × 2048 (V), sensor size: type 1.2, (Allied Vision Technologies GmbH, Stadtroda, Germany), equipped with two Nikon 28-85 mm F-mount lenses by two C to F-mount adapters (for lenses, Nikon, Tokyo, Japan), which allow for the adjusting of aperture, focus, and zoom, were mounted on a tripod and used in the experiments. Both two lenses provide an average magnification of 10 pixel/mm. One of the cameras was precisely positioned with its lens perpendicular to the focused surface of the lattice sample during the experiments. The other camera's lens was positioned at 25° to the primary camera. The testing images were captured at the rate of one frame per second, with each frame capturing a compression displacement at around 8 μm and a tension displacement around 33 μm according to the loading speed of 0.5 and 2 mm/min, respectively. The specimens were sprayed with black and white paint (Rust-Oleum, Evanston, IL, USA) to form a scattered speckle pattern on the focused surface with an average diameter of speckles of about 1.3 mm (approximately 5 pixels). Before capturing testing images, a calibration target card with 8 × 8 dots was imaged

simultaneously by rotating to different angles in both cameras to calibrate the system in one step thoroughly.

3.3.2 MTS Machine Setting

The displacement-controlling mode was applied on all the tests using a servo-hydraulic mechanical testing system (MTS 810, MTS, Eden Prairie, MN, USA). The crosshead speed was 0.5 mm/min for compression tests and 2 mm/min for tension tests, leading to a strain rate of $6.673 \times 10^{-4} s^{-1}$ for both compression and tension experiments. The tensile tests went to fracture whereas the compressive tests went until the maximum load limit of the mechanical testing frame (100 kN). In the case of the tensile tests, the specimen elongation was monitored using a standard strain gauge extensometer with a 50 mm gauge length.

3.3.3 Experimental Validation of FEA and DIC Results

Experimental validation is further demonstrated for lattice, bulk, and composite specimens. Uniaxial compression and tension tests at room temperature were conducted on all the experimental specimens. Lattice and bulk specimens are discussed apart from the bimetallic composite samples.

3.3.3.1 Validation for Lattice and Bulk Specimens

The experimental 316L stainless steel data was obtained from [111]. Overlapping the FEA compression plot in Section 3.2.1 to this experimental plot, we then obtained the final comparison plot between the FEA result and experimental result for all bulk and lattice specimens shown in **Figure 15**. We can see that for the three materials, the FEA results and experimental results are in conformance with each other, with average calculated numerical deviations of 9.8% and 5.0% for yield stress and ultimate compressive stress, respectively. Although the general shape of the

Lattice-28.82%-316L with Lattice-28.82%-316L-FEA curves are in agreement, in certain areas, the curves show a difference. This difference becomes more apparent as the plastic deformation increases. These differences occur due to unavoidable manufacturing and material defects, such as microporosity, surface roughness, deviation from the nominal dimensions, and the offset of the strut axes from the ideal axes. These variations will affect the mechanical strength of samples. Macrostructure based finite element model as presented in this work has not integrated these defects. Therefore, consequently, the FEA results are overestimated compared to the corresponding experimental results. As the specific sample is a lattice structure with a high volumetric void ratio, these errors seem higher. However, as is apparent in **Figure 15**, as the void volume ratio decreases, these errors also significantly decrease. These errors also decrease as the plastic deformation progresses towards the end where the sample densification occurs. Moreover, it is also obvious that the yield and ultimate compressive stress of 316L stainless steel lattices are less than those of both the bulk aluminum and the bulk 316L stainless steel, which means the strength of the lattice with a volume fraction of 28.82% is significantly less than the solid samples due to low volume fractions. The ultimate compressive stress, which represents the compressive strength of the lattice, can be significantly enhanced by increasing the lattice strut diameter [45]. Furthermore, the cracks in the micro-structure of the lattice can also explain the much lower yield stress and compressive strength.

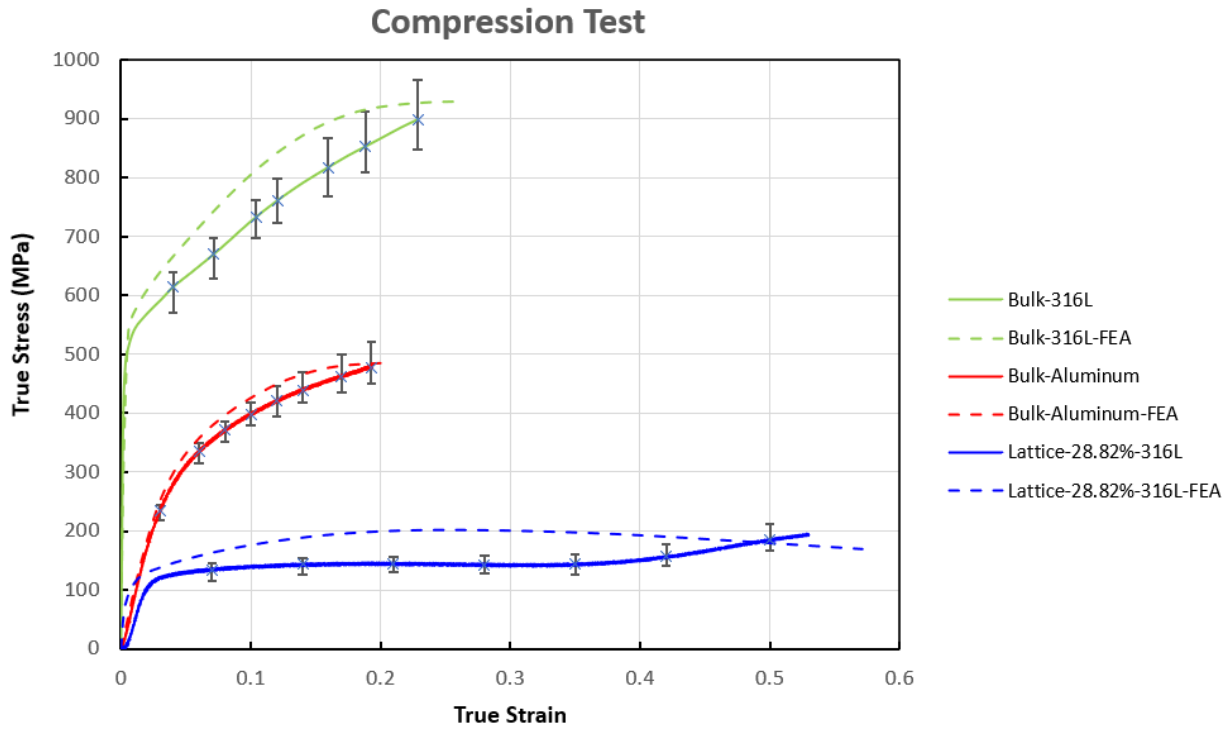

Figure 15. Comparison between experimental and FEA results of bulk 316L stainless steel, bulk dissolvable aluminum, and 316L stainless steel lattice for the compression test.

Moreover, **Figure 15** shows that the compression test for bulk aluminum stopped much earlier than the 316L stainless steel lattice counterpart. This is due to the test being stopped at the load limit (100 kN) of the mechanical testing machine before the specimen failure, while the 316L stainless steel sample collapsed before the test stopped. Three significant deformation stages, which are the elastic stage, plateau stage and densification stage, are shown in the 316L stainless steel compressive curve compared with the bulk aluminum. Initially, lattice struts were in an elastic deformation stage under the compressive load. Then, the struts approached the yield point, and the plastic stage began, which is indicated as the plateau stage. In the plateau stage, the strut nodes were dramatically squeezed, and plastic hinges formed. Finally, the densification started since the struts were continuously compressed to the point where some were broken, while others were closely squeezed against each other.

Identically, the experimental 316L stainless steel data were also collected from [111]. In order to be consistent with the compression result and further compare with the FEA result, all the experimental engineering values were transformed to the true values by using Equations (3) and (4). Similarly, mapping the FEA tension plot in Section 3.2.1 to this experimental plot, we then obtained the final tension plot between the FEA result and experimental result for all bulk and lattice specimens shown in **Figure 16**. This plot also validates that the FEA results agree with the experimental, with average calculated numerical deviations of 2.1% and 8.9% for yield stress and ultimate tensile stress. Likewise, the yield stress and tensile strength of the 316L stainless steel lattice are much lower than the other two bulk models. Increasing the strut diameter to achieve a bigger volume fraction will also improve the tension property.

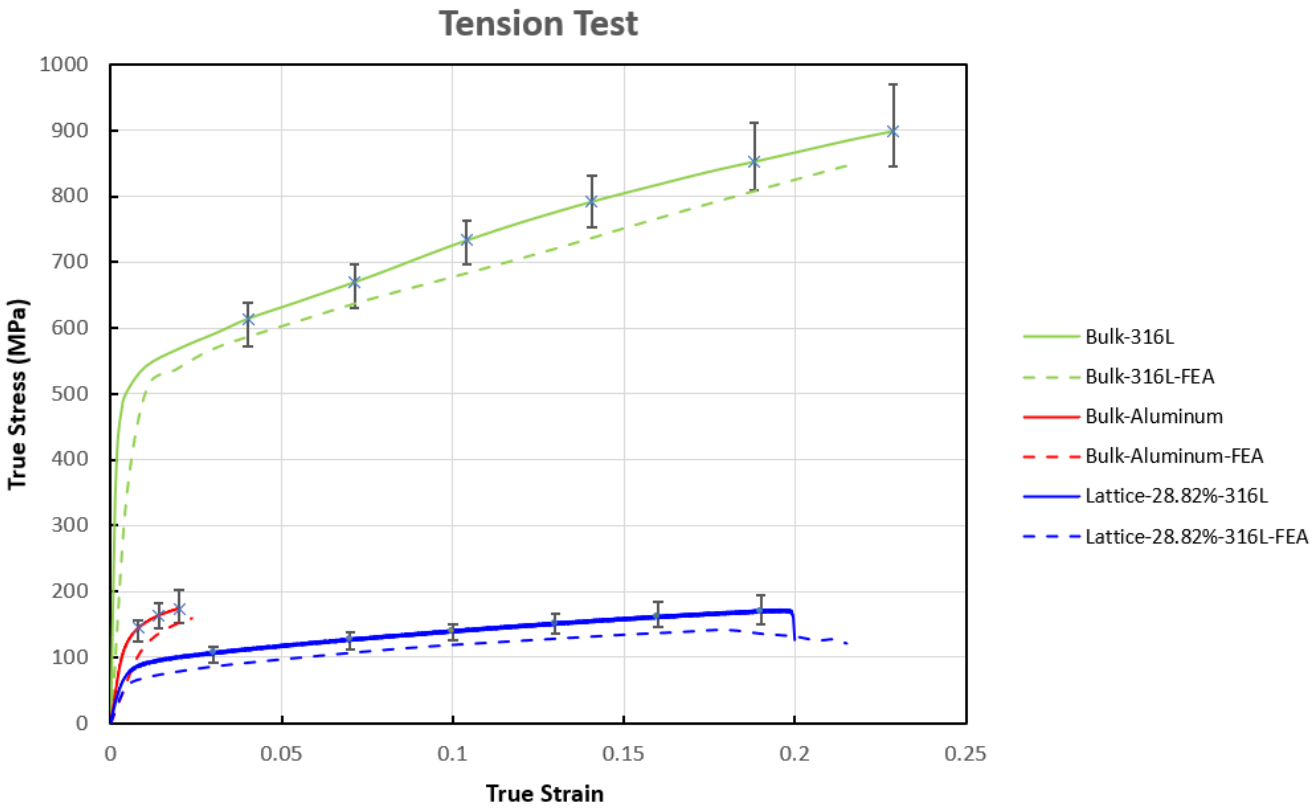

Figure 16. Comparison between experimental and FEA results of bulk 316L stainless steel, bulk dissolvable aluminum, and 316L stainless steel lattice for the tension test.

Unlike the compression testing, which has three deformation stages, the 316L stainless steel lattice just experienced the initial elastic stage and the elongational plastic stage, followed by fracture failure with a sudden drop in stress eventually. Moreover, the tensile behavior of the bulk aluminum exhibits an apparent difference from the other two, with a higher Young's modulus than the lattice but much less elongation than the other two. This is because aluminum is more brittle and has lower resistance to the tensile loading than 316L stainless steel, making it much easier to fracture with shorter elongation. In contrast, the diamond lattice configuration achieved a much-extended elongation and can be widely used in the energy absorption structure.

As for the comparison between the experimental and DIC results, we discuss the compression bulk aluminum and tension 316L stainless steel dog-bone lattice samples for brevity. A detailed view of bulk aluminum compression experimental curve is shown in **Figure 17**. Three unique points, namely the yielding point, the point in the plastic region, and the point in the hardening region, were marked out with their true strain and true stress values. The corresponding DIC images to these points are shown in **Figure 18**.

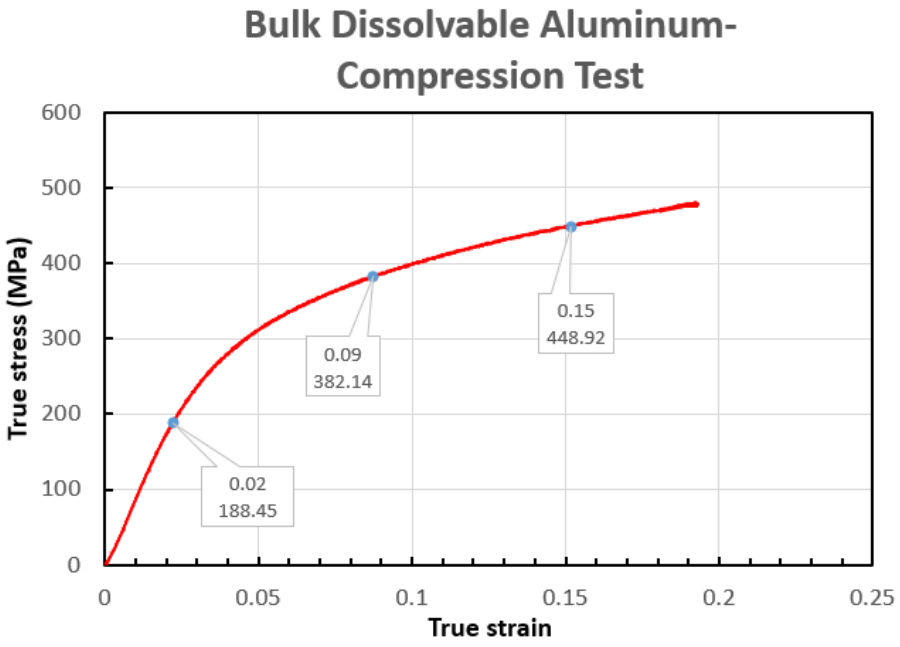

Figure 17. The experimental result of compression bulk dissolvable aluminum cube with three unique points marked out with true stress and true strain.

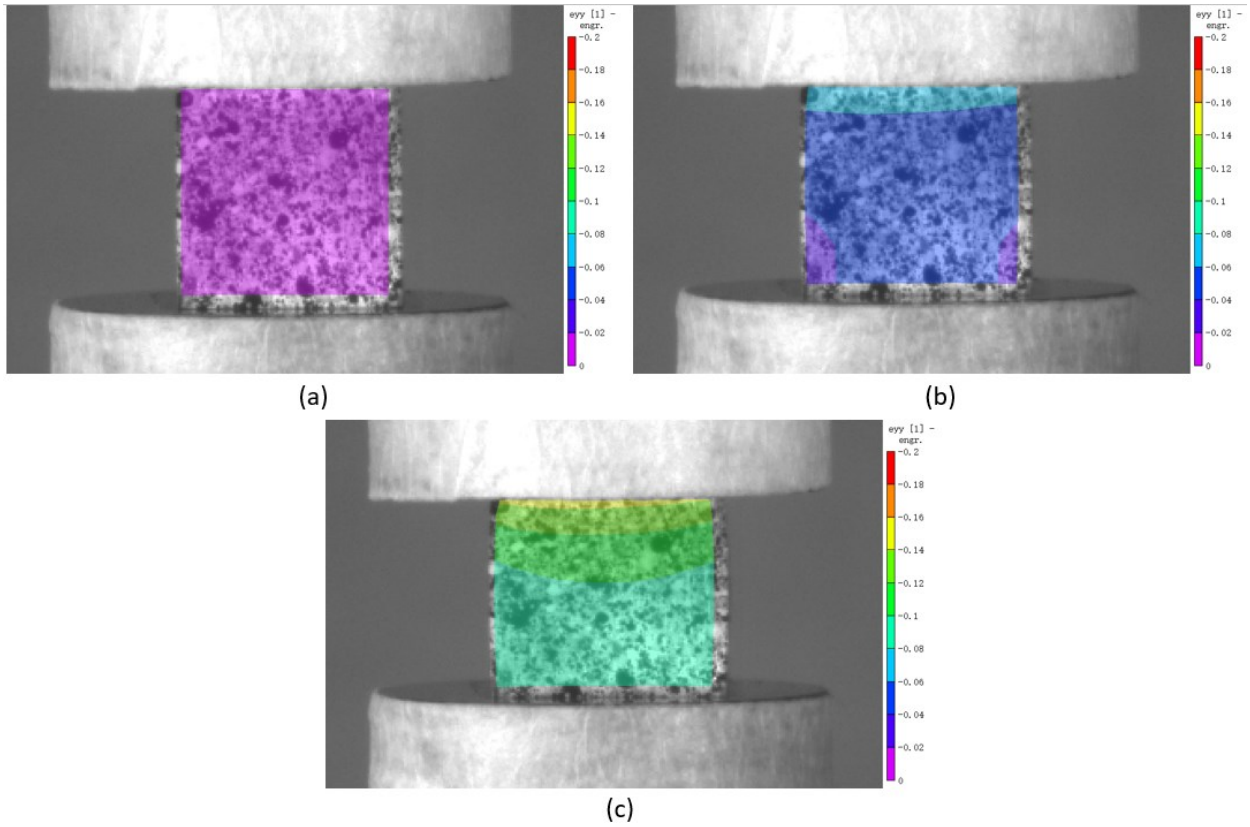

Figure 18. DIC frames of the three points marked out in the bulk dissolvable aluminum compression curve: (**a**) 34 s; (**b**) 131 s; (**c**) 228 s.

The scale bar is listed on the right side of each picture, with the strain range of −0.2 to 0 (negative values represent the compression test). From the frames, we can see that the color symbolizing engineering strain changes with loading progression, and the experimental results match the value range as the frames plotted. **Figure 18**(a) shows a uniform strain distribution as there is no severe displacement but with the increase in displacement, clear and uneven distribution can be observed in the subsequent **Figure 18**(b), (c).

Similarly, four particular points, namely the yielding point, the turning point, the point in the plastic region, and the point before the curve drop, are marked out on the tension test experimental curve of the 316L stainless steel dog-bone lattice in **Figure 19**, with corresponding DIC images shown in **Figure 20** in an increasing strain sequence, with strain ranging from 0–0.2. **Figure 20**(a)–(d) show the DIC images corresponding to the four points on the stress strain curve, obtained through the tensile testing machine using an extensometer. DIC shows slightly uneven distribution of the strain within the sample gauge length. The highest strain obtained from DIC matches the result from extensometer well. It can also be observed from **Figure 20**(c), (d) that the strain at the end of the lattice, where it attaches to the solid part of the sample is uneven and much less. This is in accordance with the expectation as the strain decreases with the increasing part density.

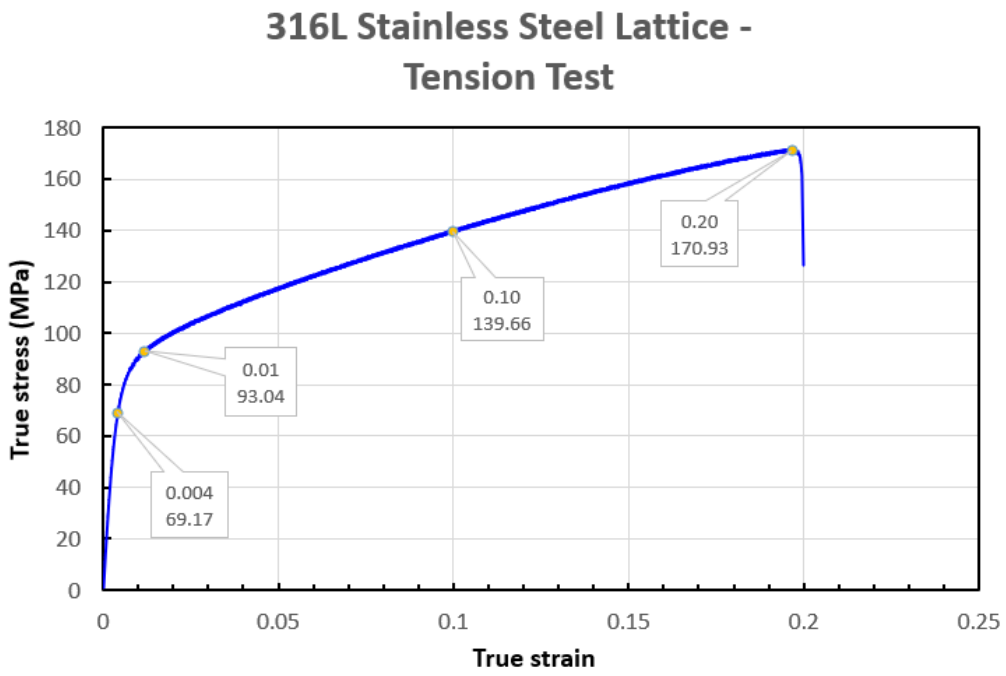

Figure 19. The experimental result of tension 316L stainless steel dog-bone lattice with four unique points marked out with true stress and true strain.

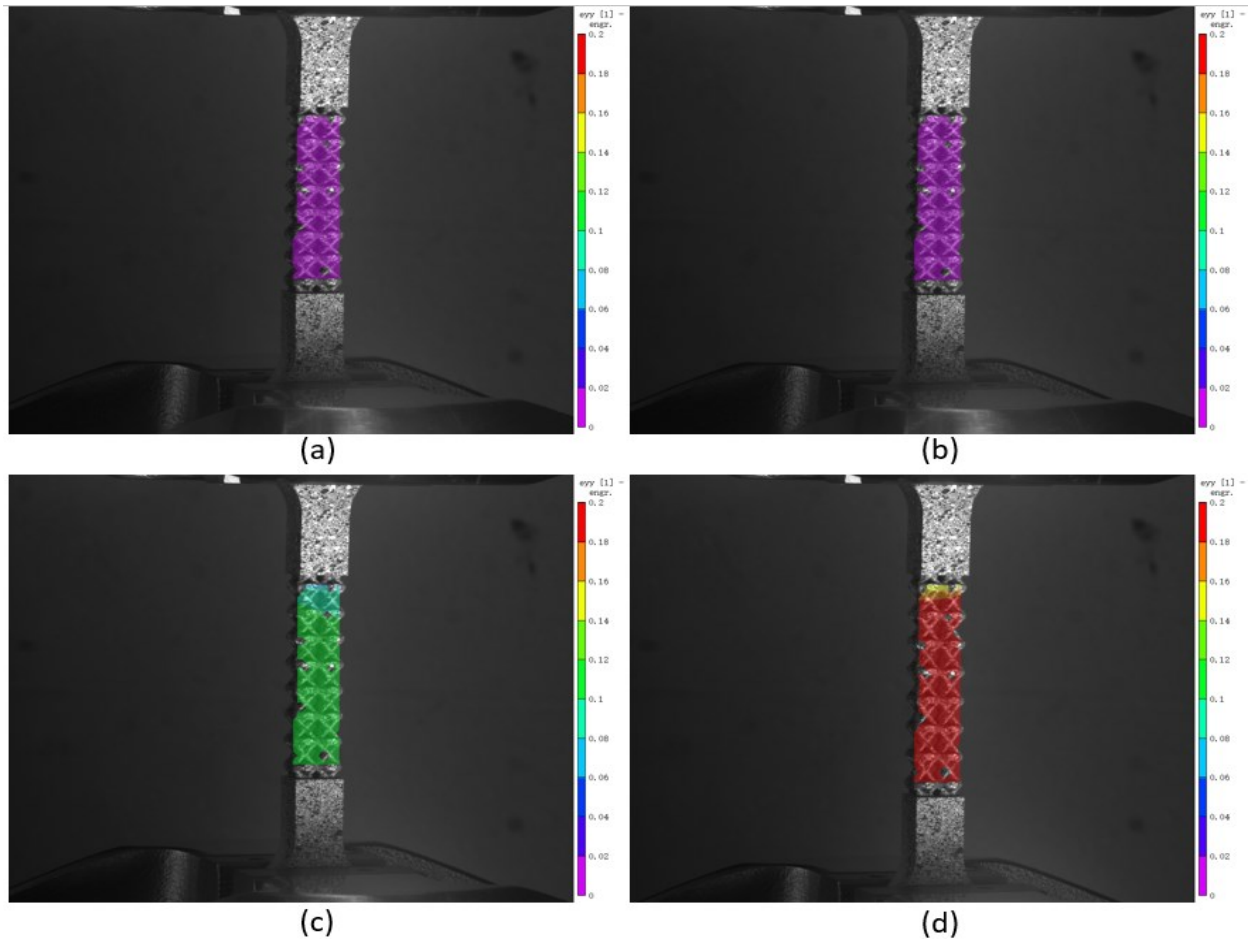

Figure 20. DIC frames of the four points marked out in the tension 316L stainless steel dog-bone lattice curve: (**a**) 6 s; (**b**) 18 s; (**c**) 150 s; (**d**) 295 s.

3.3.3.2 Validation for Bimetallic Composite Specimens

"True stress" vs. "True strain" curves of experimental results of the composite at room temperature as well as FEA results are plotted with other results of bulk and lattice samples in **Figure 21** and **Figure 22** for compression and tension tests, respectively.

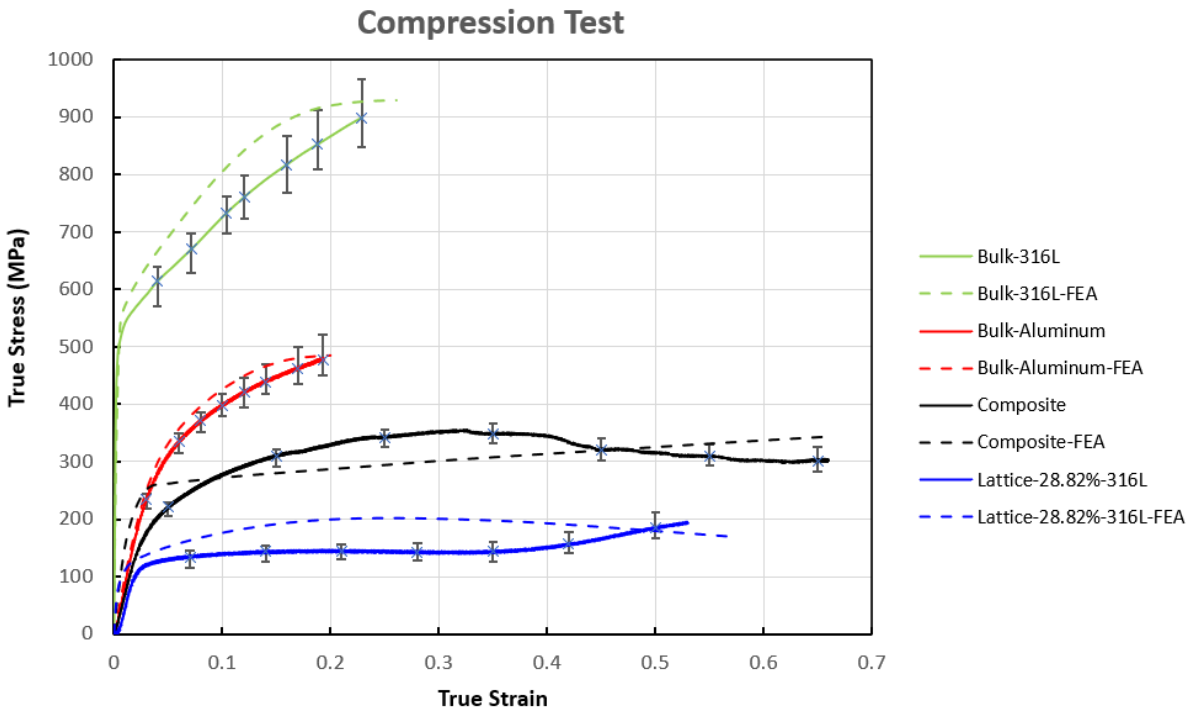

Figure 21. Comparison between experimental and FEA results of bulk 316L stainless steel, bulk dissolvable aluminum, 316L stainless steel lattice, and 316L stainless steel/dissolvable aluminum composite for the compression test.

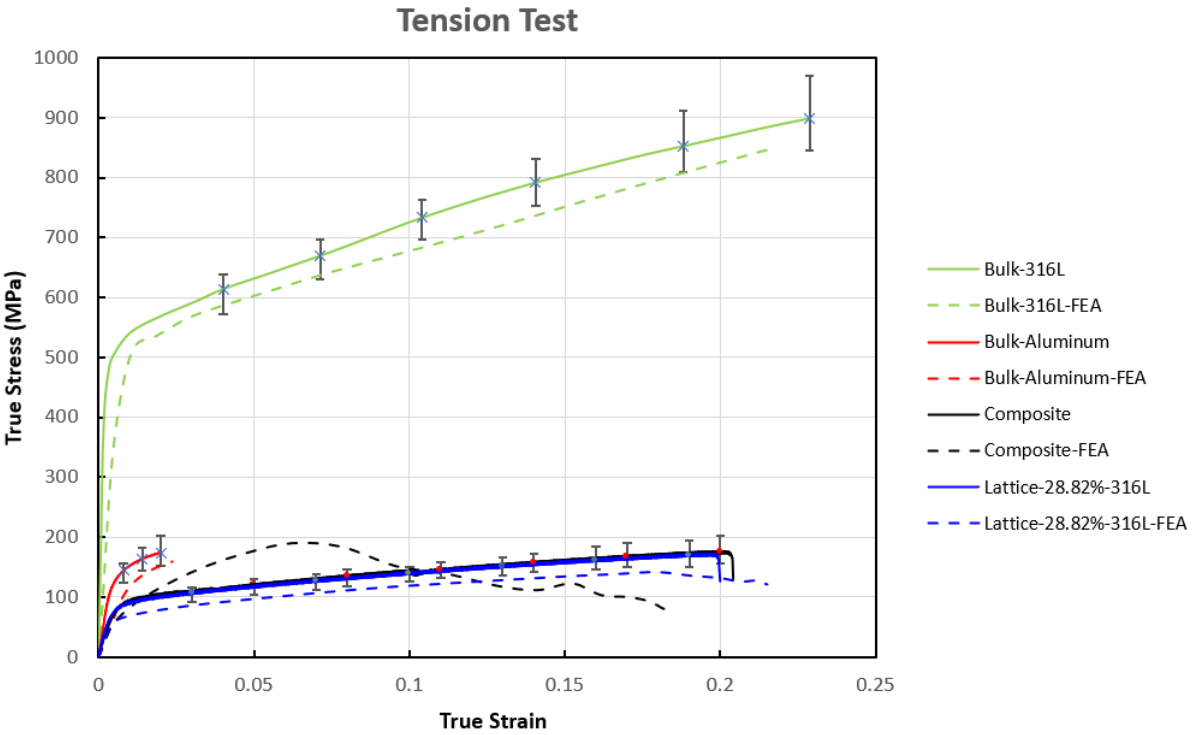

Figure 22. Comparison between experimental and FEA results of bulk 316L stainless steel, bulk

dissolvable aluminum, 316L stainless steel lattice, and 316L stainless steel/dissolvable aluminum composite for the tension test.

In terms of composite tests, there is a lack of bonding between the aluminum matrix and the SS316 lattice. This lack of material bonding plays a role in the experimental results of the compression as well as tension samples. This interface in the FEA is modeled as a hard contact with a corresponding friction coefficient. This coefficient is a constant value in the model. In the experimental tests, based upon the nature of test, i.e., compression, or tension, the interface between the two materials evolves as a function of strain and loading condition. Based on these differences it can be observed that the FEA results underestimate the compression and overestimate the tension. However, despite these, the calculated numerical deviation of 2.0% for the ultimate compressive stress confirms that the FEA simulation shows a good accuracy. Moreover, it is also apparent from the plot that the yielding and ultimate compressive strength has been significantly enhanced from the lattice shown in blue to the composite shown in black due to the filled-in matrix part. Nonetheless, the mechanical properties of the composite are less than the bulk aluminum properties shown in red. This can be addressed by increasing the volume fraction of the lattice. Using the rule of mixtures, this would result in composite properties between the lower bound of bulk aluminum and the upper bound of bulk 316L stainless steel.

Composite compression and tension experimental curves were taken out of the plots shown in **Figure 23** and **Figure 24**. For the compression test, as clarified in Section 3.3.3.1, three unique points, namely the yield point, a point in the plastic region, and a point in the hardening region, were marked out with their true strain and true stress values, and the corresponding frames captured by the DIC system are shown in **Figure 25**. In contrast, for the tensile test, four points, namely the yield point, a point in the plastic region, a point before the first curve dip, and the last point that the DIC effectively tracked, were marked out, and the DIC results were shown in **Figure 26**. The

corresponding time calculated for the compression test was 35, 179, and 383 s, while 9, 21, 54, and 101 s for the tension test.

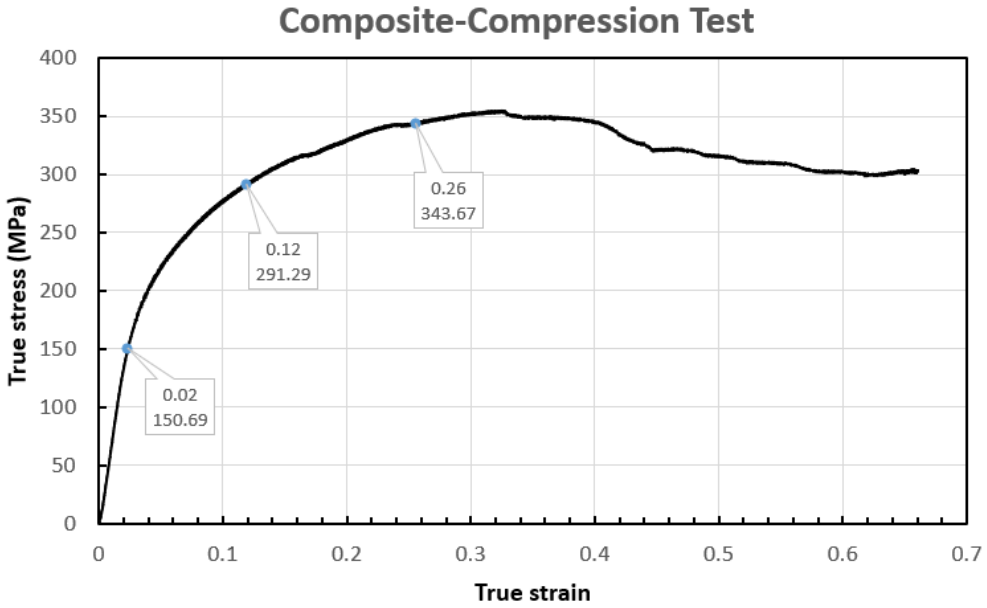

Figure 23. The experimental result of compression composite cube with three unique points marked out with true stress and true strain.

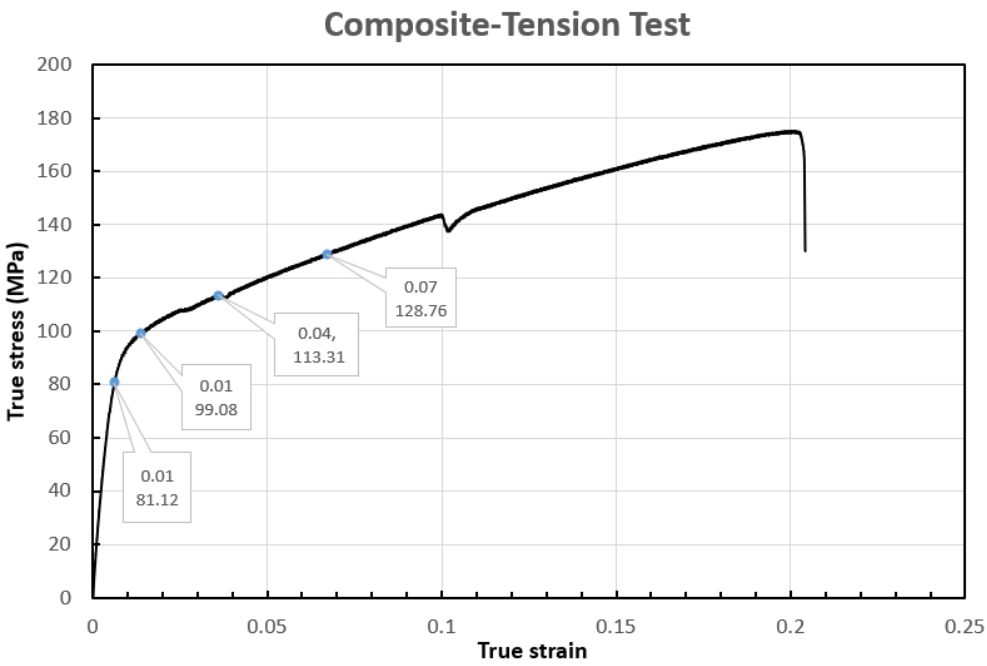

Figure 24. The experimental result of tension composite dog-bone with four unique points marked out with true stress and true strain.

The tension results are different from the compression curves, where two distinct regions can be found in the experimental results, the elastic region, and plastic region, after which a sudden drop is shown, indicating the rupture of the sample. It is significant to note that the tensile curves for the 316L stainless steel lattice and bimetallic lattice are similar. This indicates that the aluminum matrix does not play an essential role due to lack of bonding. Similar to the compression results, the bulk 316L stainless steel and bulk aluminum possess higher yield stress and ultimate tensile stress, and both tensile curves of the 316L lattice and composite do not even surpass the curve of bulk aluminum. However, the dissolvable aluminum presents a much lower elongation comparing to the other three samples. The trivial difference between the experimental and FEA data for all four pairs validates the simulation results, including the numerical calculated deviation of 2.0% for the ultimate stress of the tension composite. The ABAQUS™ simulation curve for the bimetallic composite generally matches the results from Cheng et al. [72].

The DIC data for compression and tension tests of composite samples reveal that the strain pattern is uneven along the length of the sample. This is in departure from the DIC test results for the bulk aluminum, as well as the SS316 lattice structure, which showed a more even strain distribution as compared to the composite samples.

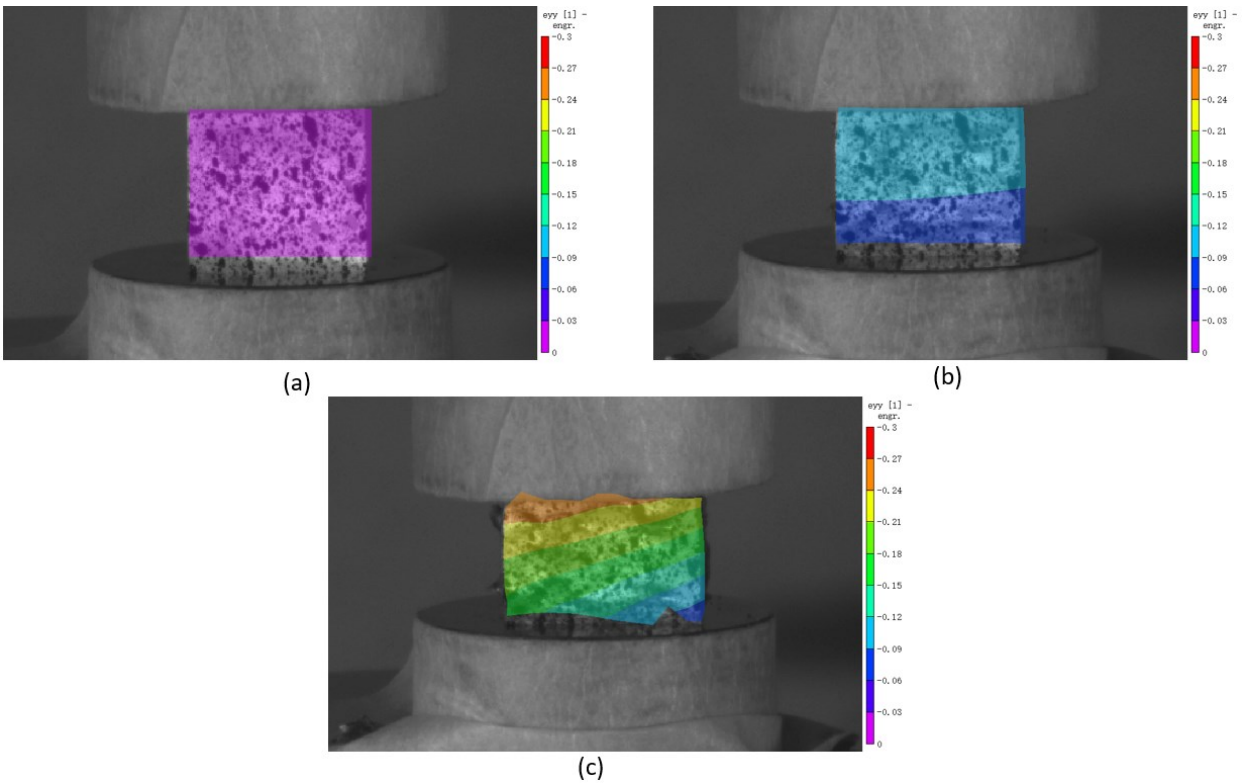

Figure 25. DIC frames of the three points marked out in the composite compression curve: (**a**) 35 s; (**b**) 179 s; (**c**) 383 s.

A strain range of -0.3 to 0 (**Figure 25**) was exhibited in the compression and 0 to 0.1 (**Figure 26**) in the tension. The strain behavior of the compression composite represented by the color coding was very similar to the bulk dissolvable aluminum. However, slight differences were observed for the tension composite. The strain growth was observed to grow gradually from the center to both sides, initially from 0 shown as purple color in the first frame to about 0.07 with orange color appearing in the middle part of the last frame. Experimental strain results of the curve plots (**Figure 23** for compression and **Figure 24** for tension) match the value range plotted in the frames for both the compression and tension composite samples.

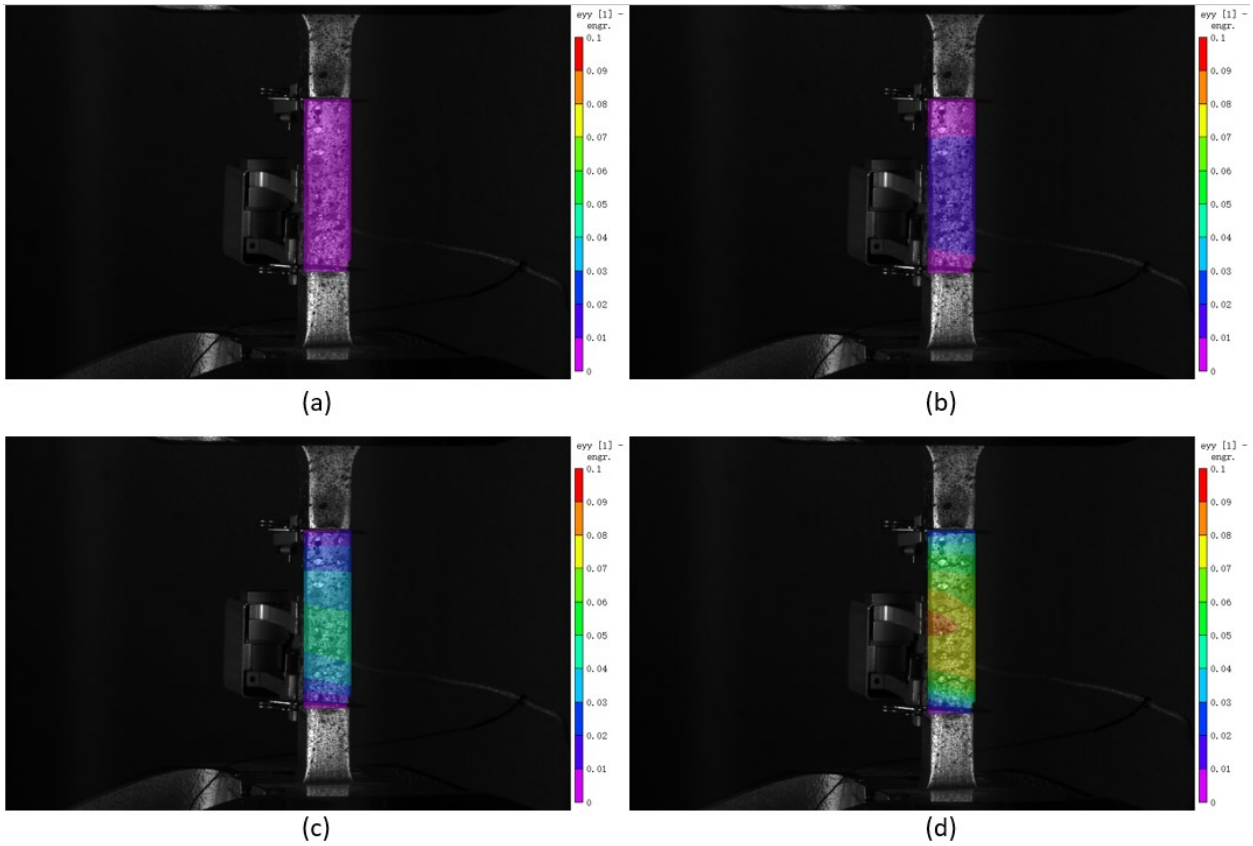

Figure 26. DIC frames of the four points marked out in the composite tension curve:

(**a**) 9 s; (**b**) 21 s; (**c**) 54 s; (**d**) 101 s.

CHAPTER 4

GEOMETRIC ANALYSIS OF CT SCANNING DATA OF ADDITIVE MANUFACTURED SAMPLES AND NOMINAL MODELS

This chapter investigated six types of compression and tension lattice-structured samples with different volume fractions, namely 28% compression lattice, 70% compression lattice, 28% tension lattice, 70% tension lattice, bulk compression, and bulk tension, in which 28% and 70% are the two different varieties of volume fractions in the specimens. The volume fraction of the lattice structure is defined as the volume ratio of the lattice structure to the entire space that the lattice structure occupies, and can also be explained as the volume ratio of one unit cell to the cubic space that the unit cell resides. Furthermore, if the volume fraction reaches 100%, the structure becomes a solid and bulk part, which is not latticed anymore. Bulk compression and tension samples were also included besides the lattice structures in the study for accuracy, comparison and verification of the MicroCT results. The aim is to characterize and compare the porosity and shape deviation results of samples with lattice structures of different volume fractions.

4.1 SolidWorks Modelling

The Diamond unit cell selected for the lattice model for CT scanning is the same as introduced and applied in Chapter 2. All models with either lattice structures or bulk parts were made by SolidWorks™. Compression lattice samples were in the shape of a cube with a height of 12.5 mm, with lattice strut diameters of 2 mm and 3.74 mm for 28% and 70% models, respectively. The length, width and height of the unit cell are equally to be 6.25 mm; hence, in order to form a 12.5

mm cube model, the linear pattern was applied with the amount of two unit cells in each direction. Therefore, the compression lattice model was created by stacking 8 unit cells together, which was exactly the same as the compression model in Chapter 2. However, unlike the compression models, tension models should be made as dog-bone shapes, conforming to the ASTM E8M standard [30] with a gauge length of 31.25 mm, a gauge width of 12.5 mm, and a total length of 80 mm. We decreased the overall length of the tension model from 140 mm in Chapter 2 to 80 mm here because we would like to print the samples using the 3D printer in our lab and 80 mm is the maximum length that can be printed. Detailed dimensions for the 28% tension model as an example are demonstrated in **Figure 27**. The thicknesses of the lattice strut remained the same at 2 mm and 3.74 mm as the compression models. 0.75 mm fillets were designed on the junction interface of grips to reduce stress concentration and prevent failure in this area. Dimensions of bulk compression and tension models followed the same overall length, height and width compared to the lattice ones, except that only the lattice part was fulfilled with the solid structure instead of the stacking-up unit cells. **Figure 28** plots the computer-aided design (CAD) models of 28% and 70% compression and tension samples for the lattice and bulk material.

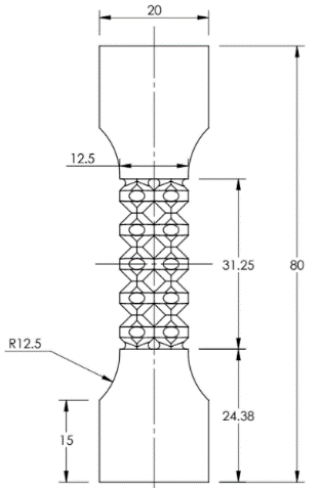

Figure 27. Tension test sample with 28% diamond lattice structures embedded in the gauge length.

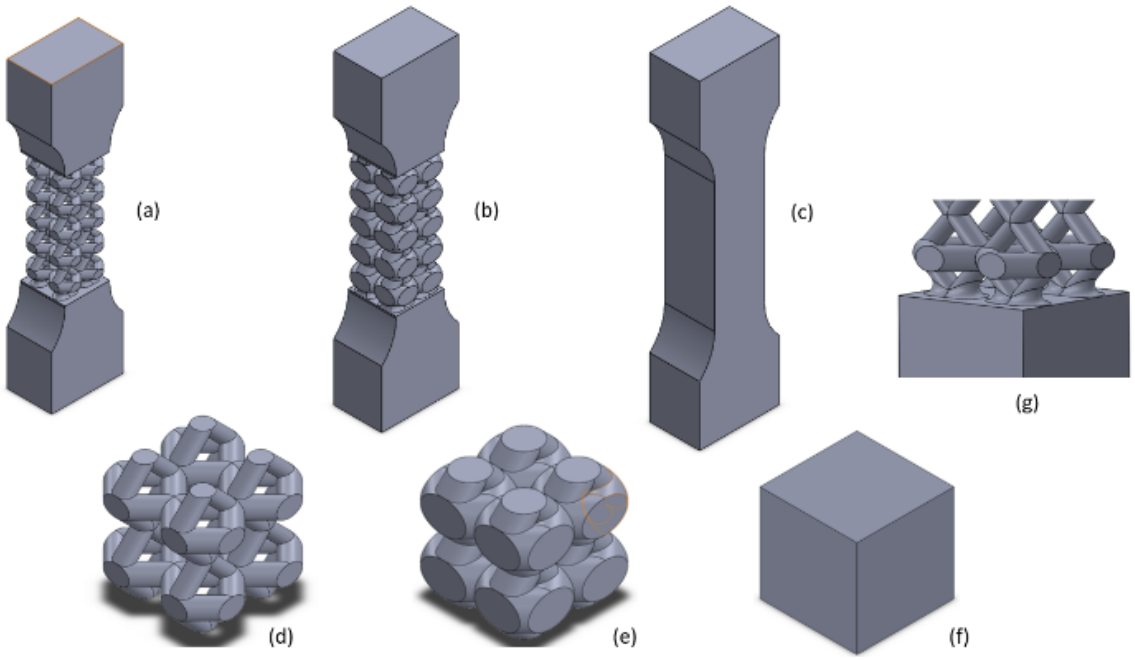

Figure 28. Computer-aided design (CAD) models of 28% and 70% compression and tension samples for lattice and bulk: (**a**) 28% tension lattice; (**b**) 70% tension lattice; (**c**) bulk tension; (**d**) 28% compression lattice; (**e**) 70% compression lattice; (**f**) bulk compression; (**g**) fillets in the interface of tension dog-bone model.

4.2 Materials and Manufacturing

Both 17-4PH and 316L stainless steel were applied to additively manufacture the samples through laser powder bed fusion (LPBF) fabrication. The argon-gas-atomized 17-4PH stainless steel powder with a 15-45 μm particle size range was fed for the LPBF process. The chemical composition of 17-4PH stainless steel powder is listed in **Table 3**. The 17-4PH stainless steel samples were printed through the CREATOR 3D metal printer (Coherent, Inc., California, USA) in our lab, which directly builds metallic parts and components with highly complicated geometries and structures eliminating the requirement for mould tools. The 250 W internal fiber laser offers superior beam quality and performance stability, and the inside building chamber features a unique coating operation with powdered materials, enabling accelerated build speeds [112]. An alternating scan pattern was applied to all the lattice parts. The hatching direction of

each layer was rotated by 45° from that of the previous one. High-purity argon gas was purged into the building chamber to maintain an oxygen level of about 0.01% during the printing process. Besides, the temperature in the building chamber was maintained in the range of 25 - 40 °C.

Table 3. Chemical composition of 17-4PH stainless steel powder used as the feedstock material for the LPBF process (wt.%).

Chemical Composition	Fe	Cr	Ni	Cu	Nb+Ta	C	Other
Value (wt.%)	Balance	17	4.5	4.0	0.3	< 0.07	< 1.0

The solution heat treatment was applied for the post-processing. The 17-4PH specimens were heated to 1050 °C for 1 hour hold time, then water-quenched, followed by the ageing heat treatment at 482 °C for 1 hour, and finally processed by air cooling. The ageing heat treatment aims to increase strength and hardness by producing the precipitation of fine copper.

Table 4. Chemical composition of SS 316L - 0407 powder used as the feedstock material for the LPBF process (wt.%).

Chemical Composition	Fe	Cr	Ni	Mo	Mn	Si	N	O	P	C	S
Value (wt.%)	Balance	16 - 18	10 - 14	2 - 3	≤ 2	≤ 1	≤ 0.1	≤ 0.1	≤ 0.045	≤ 0.03	≤ 0.03

The low-carbon SS 316L - 0407 powder was served as the feedstock for the LPBF process of 316L samples. 316L - 0407 is resistant to sensitization and exhibits good welding characteristics. The chemical composition of SS 316L powder is listed in **Table 4**. The 316L stainless steel samples are printed by Renishaw AM250 Printer (Renishaw, Gloucestershire, UK) for LPBF techniques. This printer is mainly designed to construct medium-sized components with high precision and surface quality. It is also compatible with other types of powder besides stainless steel, such as Inconel, Cobalt Chrome, Aluminum and Titanium. Manufacturing processing parameters of the CREATOR 3D metal printer (Coherent, Inc., California, USA) for 17-4 PH samples and Renishaw AM250 LPBF processes for SS 316L samples are both noted in **Table 5**. No heat treatment was

applied on 316L stainless steel samples.

Table 5. Manufacturing processing parameters of CREATOR 3D metal printer and Renishaw AM250 printer for fabrication of 17-4PH and 316L stainless steel samples.

Parameters	17-4 PH	316L
Laser Power (W)	107.3	50 - 180
Scan Speed (mm/s)	1000	400 - 1200
Layer Thickness (μm)	25	40
Hatch Spacing (μm)	40	90
Build Size (mm)	100 × 110 × 200	250 × 250 × 365
Hatch Pattern	Alternating	Alternating

Two images of the experimental 17-4PH and 316L stainless steel samples in this study are shown in **Figure 29**.

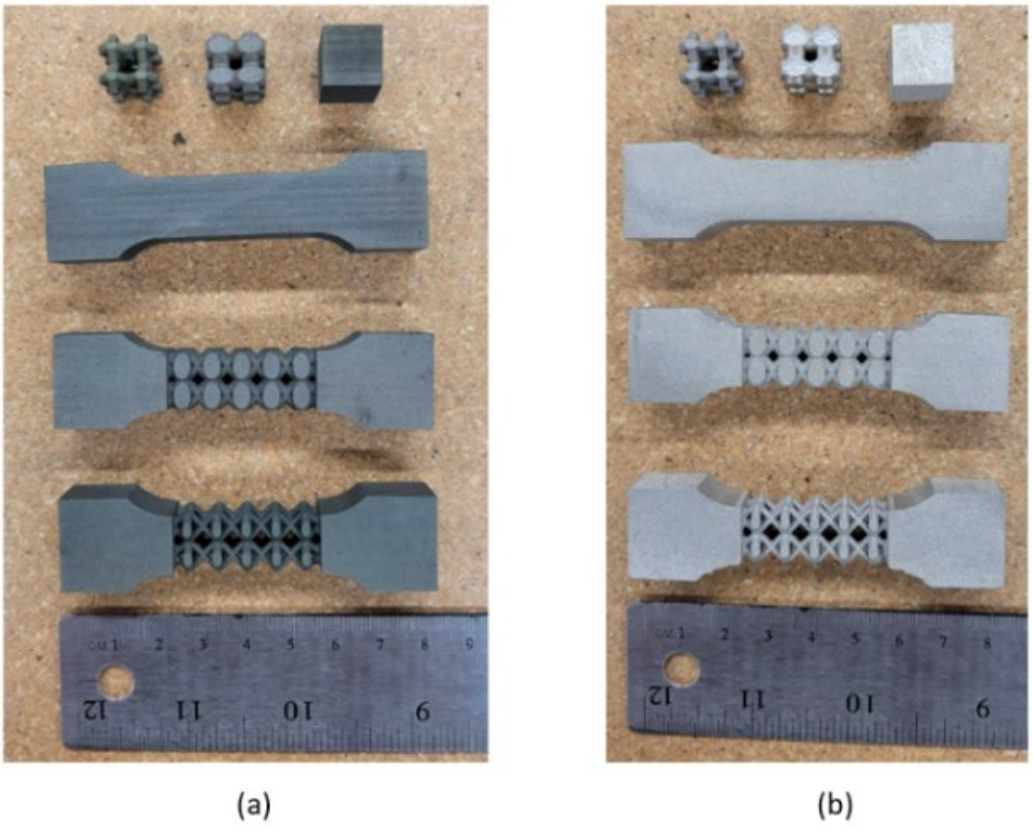

Figure 29. LPBF manufactured (a) 17-4PH and (b) 316L samples.

4.3 Characterization through X-ray Microscope Scanning

All samples were scanned by X-ray Microscopy/CT, a non-destructive characterization method, with a voltage of 160 kV. 2% - 99% X-ray was guaranteed to pass through the samples and not wholly absorbed by the pores. The resulting data was processed by ORS dragonfly Pro (Object Research Systems (ORS) Inc., Quebec, Canada) to visualize 3D shapes, position, and volumes and statistical distribution of the porosities within the microstructures. Samples were scanned by X-ray twice: firstly, output the entire 3D shapes of the sample for comparison with nominal models by applying a full scanning resolution of 53 μm/pixel on average, and secondly, further examine the inside porosities by applying detailed resolution of 8.6 μm/pixel approximately.

The 3D X-ray microscopy data was converted into point cloud data and saved in STL file format. As shown in **Figure 30** and **Figure 31**, the STL files represent the actual external shape of the manufactured samples. These files are compared with the input CAD data using a virtual inspection tool and color maps are generated. These color maps are further analyzed for geometric and shape deviation of the samples.

4.3.1 Analysis of CT Scanning Data of 316L Stainless Steel and 17-4PH Stainless Steel

The 3D shapes of the samples were exported as meshed STL files from ORS Dragonfly Pro, and the volume of the exported STL structure was compared with the nominal structure modelled by SolidWorks™. **Figure 30** and **Figure 31** show STL models of monolithic compression cube in 17-4PH and 70% lattice tension dog-bone in 316L, respectively, as two examples of the exported STL file by ORS Dragonfly Pro. The scanned model is shown at the top left of the figure, and the scanned volume is marked in the red frame. To compare the scanned STL models exported with

nominal models created by SolidWorks™, the results were summarized with the deviation listed in **Table 6** and **Table 7** for 316L and 17-4PH, respectively. The low discrepancy between the volumes proved the reliability and precision of the X-ray Microscopy scanning results.

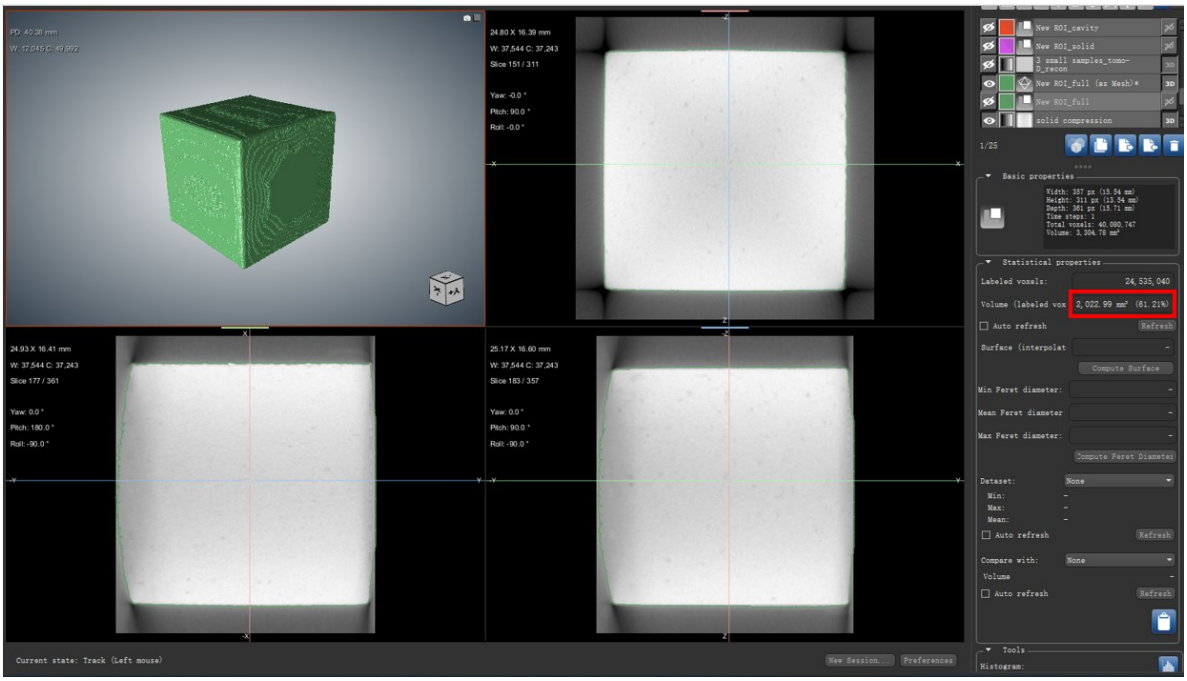

Figure 30. Isometric and orthogonal visualization of 17-4PH monolithic compression cube.

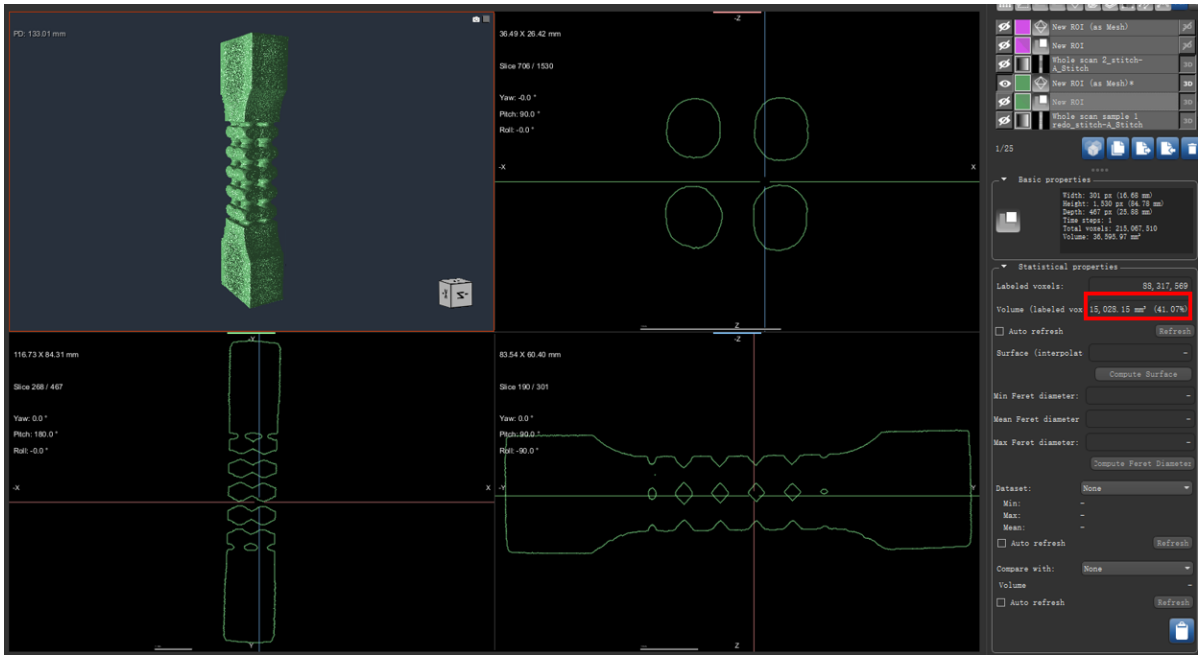

Figure 31. Isometric and orthogonal visualization of 316L 70% tension lattice dog bone.

Table 6. The volume comparison between the scanned STL models exported and nominal models created by SolidWorks™ for 316L samples.

Model Types	Exported STL Model (mm^3)	Nominal Model (mm^3)	Deviation (%)	Average Deviation (%)
70% Tension Lattice	15028.15	14429.11	4.2	3.7
28% Tension Lattice	12915.00	12383.27	4.3	
Monolithic Tension Dog Bone	16426.45	15831.98	3.8	
70% Compression Lattice	1330.02	1374.52	3.2	
28% Compression Lattice	582.73	563.05	3.5	
Monolithic Compression Cube	2022.99	1953.13	3.1	

Table 7. The volume comparison between the scanned STL models exported and nominal models created by SolidWorks™ for 17-4PH samples.

Model Types	Exported STL Model (mm^3)	Nominal Model (mm^3)	Deviation (%)	Average Deviation (%)
70% Tension Lattice	14467.67	14429.11	0.27	3.3
28% Tension Lattice	13129.35	12383.27	6.0	
Monolithic Tension Dog Bone	16233.58	15831.98	2.5	
70% Compression Lattice	1354.66	1374.52	1.4	
28% Compression Lattice	530.14	563.05	5.8	
Monolithic Compression Cube	2022.99	1953.13	3.6	

The second-time scanning was pointed to a small portion of the sample to investigate the void distribution in the material. **Figure 32** and **Figure 33** display the void distribution within 28% lattice tension dog bone sample of 17-4PH represented in blue and bulk compression cubic sample of 316L represented in orange, respectively, as two examples among the investigation of all six types of samples. To summarize the analyzing results, the porosity values of 316L and 17-4PH samples of six different types of models were listed in **Table 8**. It is worth noting that more pores were found inside monolithic samples due to the greater temperature gradient experienced during the LPBF fabrication procedure than smaller lattice samples, in which temperature was more evenly distributed with more uniform heat transmission.

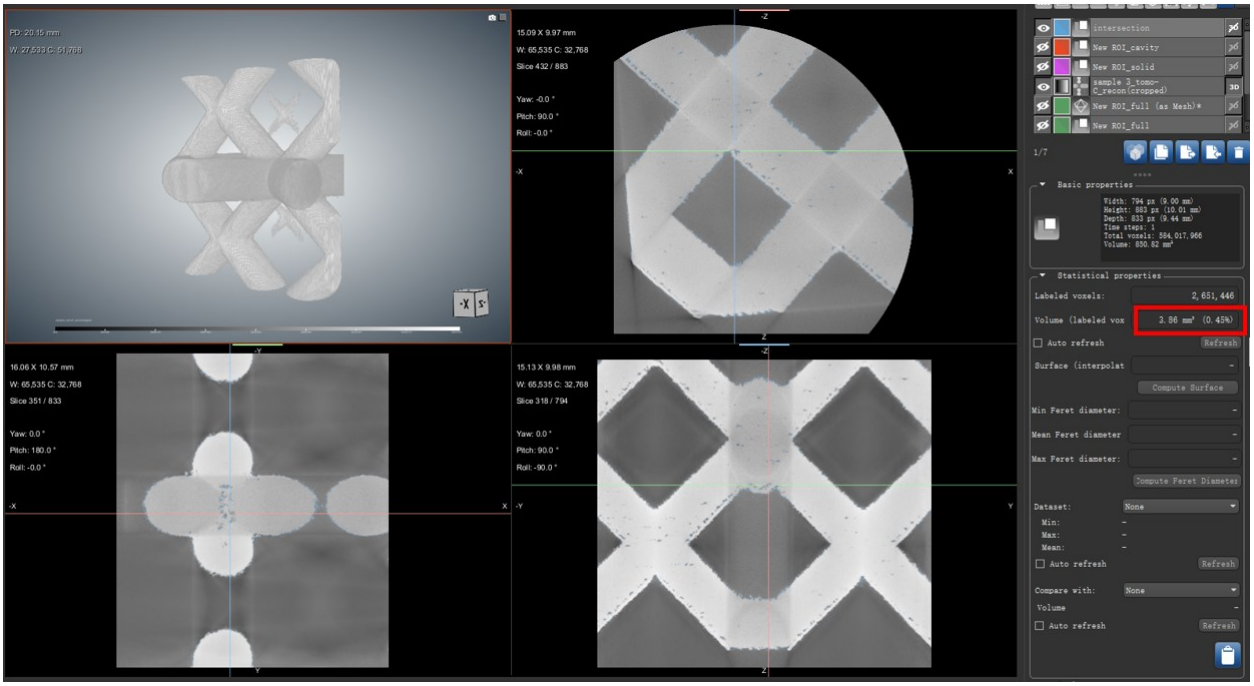

Figure 32. The percentage of pores within 17-4PH 28% tension lattice dog bone.

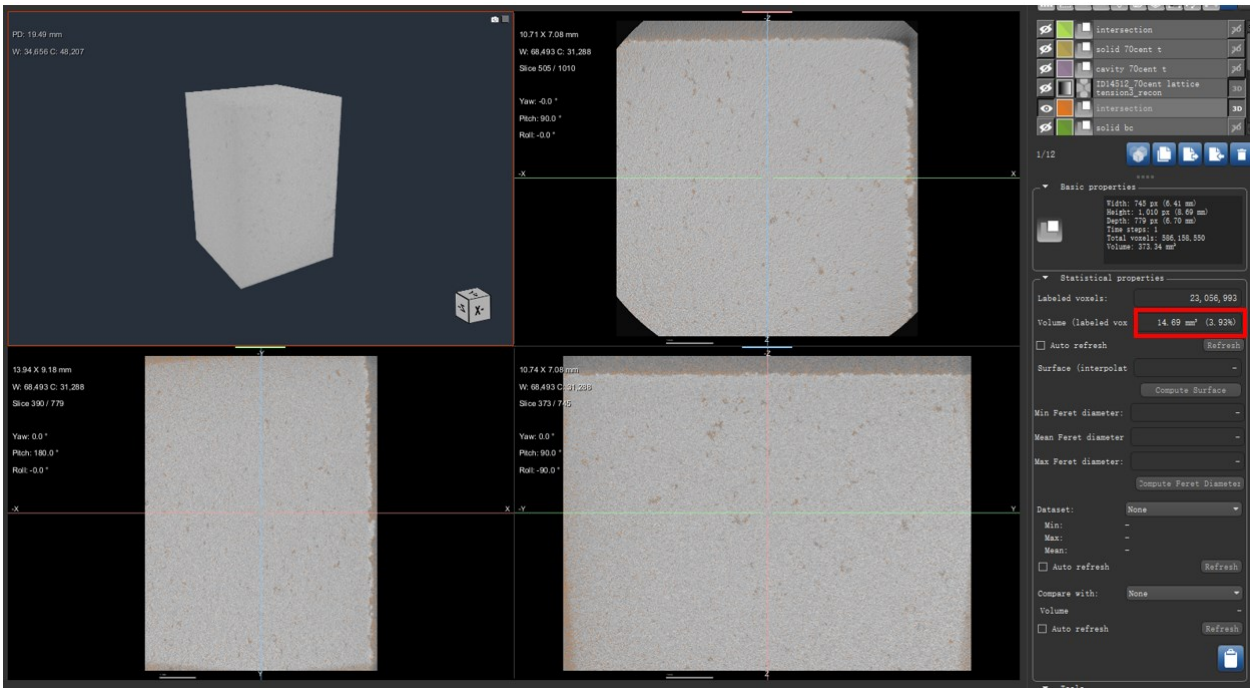

Figure 33. The percentage of pores within 316L bulk compression cube.

Table 8. The porosity percentages of 316L and 17-4PH samples for six different types of models.

Model Types	316L (%)	17-4PH (%)
70% tension lattice	0.14	0.89
28% tension lattice	0.26	0.45
Monolithic tension dog bone	3.71	0.69
70% compression lattice	1.05	0.52
28% compression lattice	0.21	0.23
Monolithic compression cube	3.93	2.21
Average Porosity Percentage	1.55	0.83

Furthermore, a cylindrical portion was extracted from the 316L monolithic compression cubic sample in Dragonfly to examine the volume, position, and statistical distribution of the pores, as shown in **Figure 34**, where different colors are used to depict different pore sizes. It is apparent that most of the pores are smaller than 0.0001 mm^3.

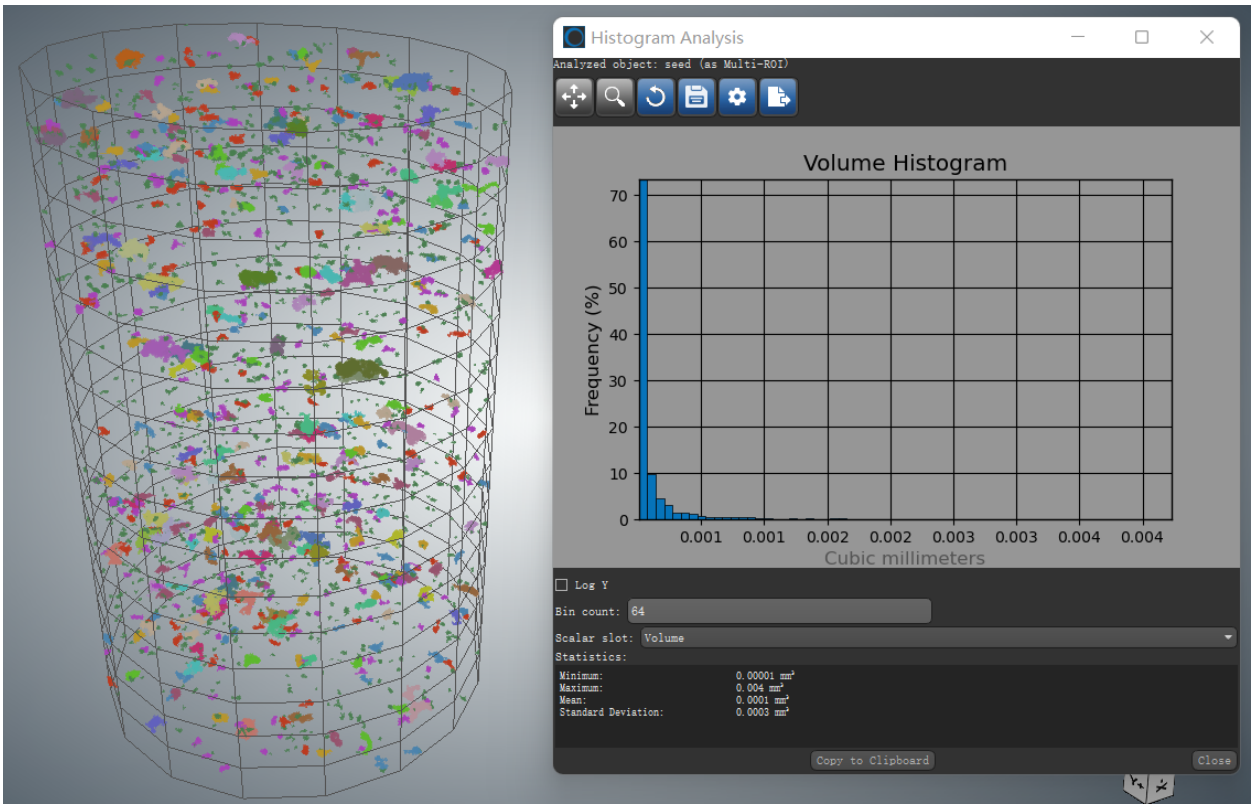

Figure 34. Volume, position, and statistical distribution of the pores inside 316L monolithic compression cube.

4.3.2 Geometric Comparison between Scanned and Nominal Geometries

The contour plots of the geometrical deviation of different samples of both material types are shown below from **Figure 35** to **Figure 38**. Overall shrinkage is observed in all the samples irrespective of the volume fraction and the geometry of the sample. As seen in **Figure 35**, the 28% lattice compression sample exhibits an average shrinkage of 1.8 mm with minor expansions in some internal regions. On the outer surface of the lattice the shrinkage is uniform and is almost to the same as the average value. However, for the 28% lattice tensile sample of 17-4 PH steel, the shrinkage was mostly observed in the gauge length region, i.e., in the area where the lattice structures are present, which was not observed in the monolithic samples (not shown). It indicates that the complex geometric shapes, i.e., lattices, have led to more shrinkage than the solid samples. This could be attributed to the fact that the small cross section of lattice beams experiences much higher thermal gradients and shrinks due to rapid solidification of the material after melting.

For the 70% lattice samples as shown in **Figure 36**, a similar scenario is observed. For the 70% lattice compression samples of 17-4 PH the average shrinkage is observed of around 3.4 mm with minor expansion in the internal regions. The external boundary of the lattice structure exhibits most significant shrinkage, particularly on the edges.

For the 70% lattice tensile sample of 17-4 PH there are prominent regions of both expansion and shrinkage in the lattice region. The expansion regions have an average expansion of around 3.4 mm and the shrinkage regions have an average shrinkage of around 3.6 mm.

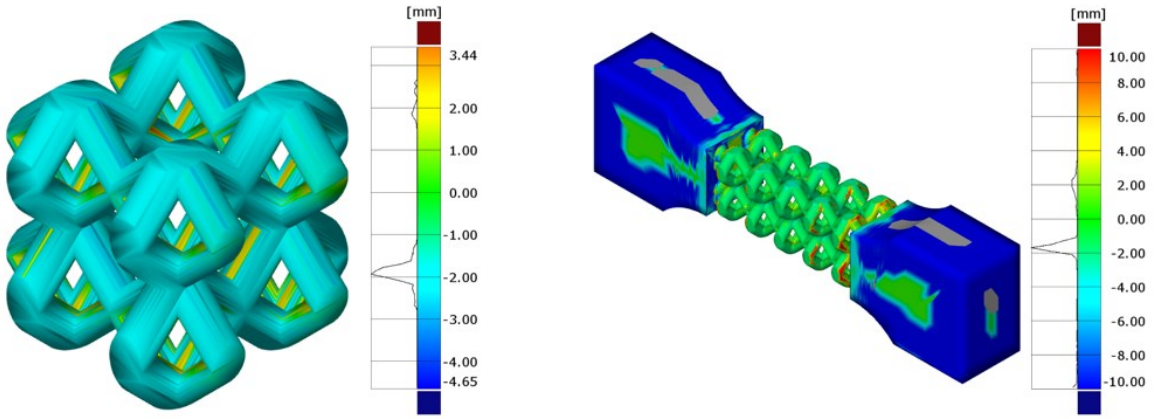

Figure 35. Shape deviation color map of 17-4 PH 28% compression and tension sample.

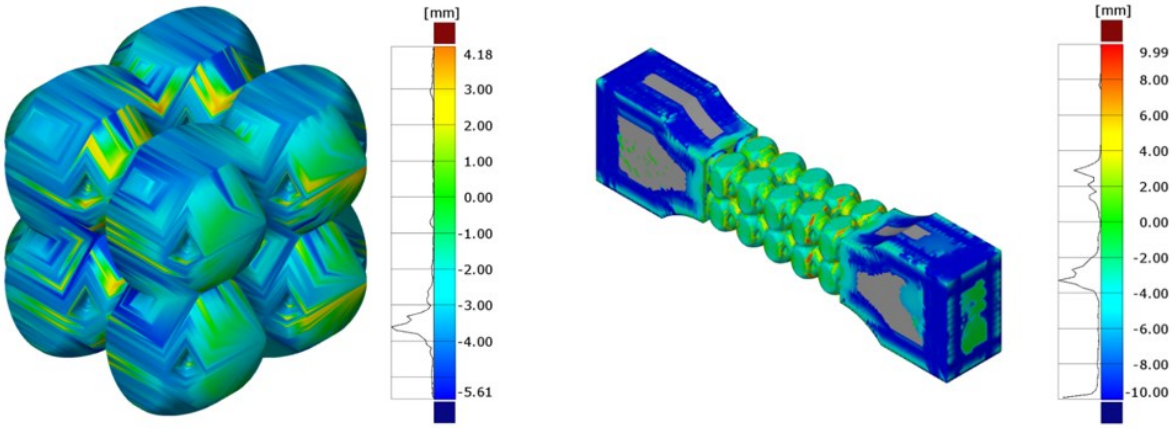

Figure 36. Shape deviation color map of 17-4 PH 70% compression and tension sample.

For 316L samples shown in **Figure 37** and **Figure 38** as well, a very similar outlook is observed. **Figure 37** shows that the 28% lattice compression sample has an average shrinkage of around 2.2 mm with minor expansion regions at the interiors. Also, the 28% lattice tension sample shows an average shrinkage of 1.8 mm. For the 70% lattice compression sample of 316L the average shrinkage is about 3.6 mm. And for the 70% lattice tensile sample both expansion and shrinkage are observed as shown in **Figure 38**. The shrinkage mode occurs because of the thermal gradients

and the related process parameters. However, shrinkage although not desirable, is not as catastrophic as sub-optimal mechanical or material properties. So, the optimization of process parameters of the LPBF process needs to consider both mechanical and geometric properties of the component to be manufactured.

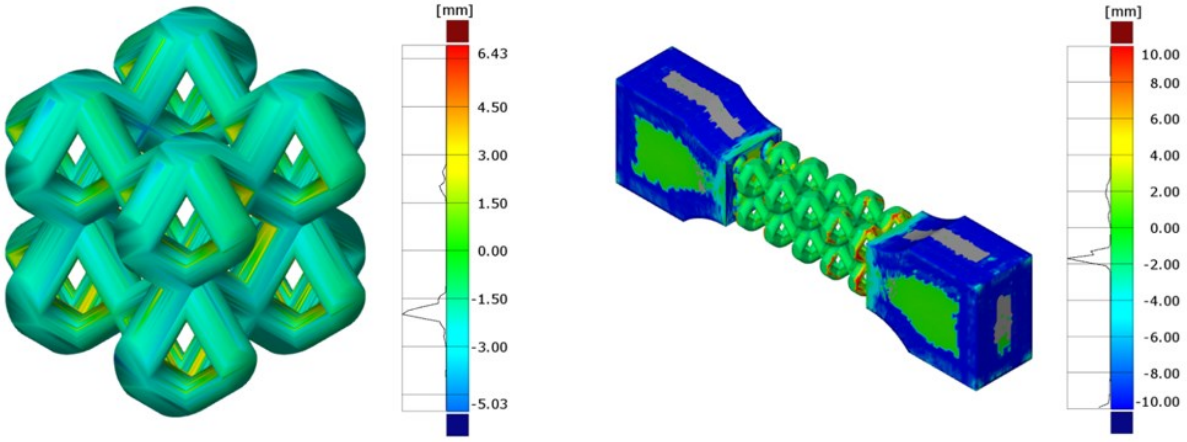

Figure 37. Shape deviation color map of 316L 28% compression and tension sample.

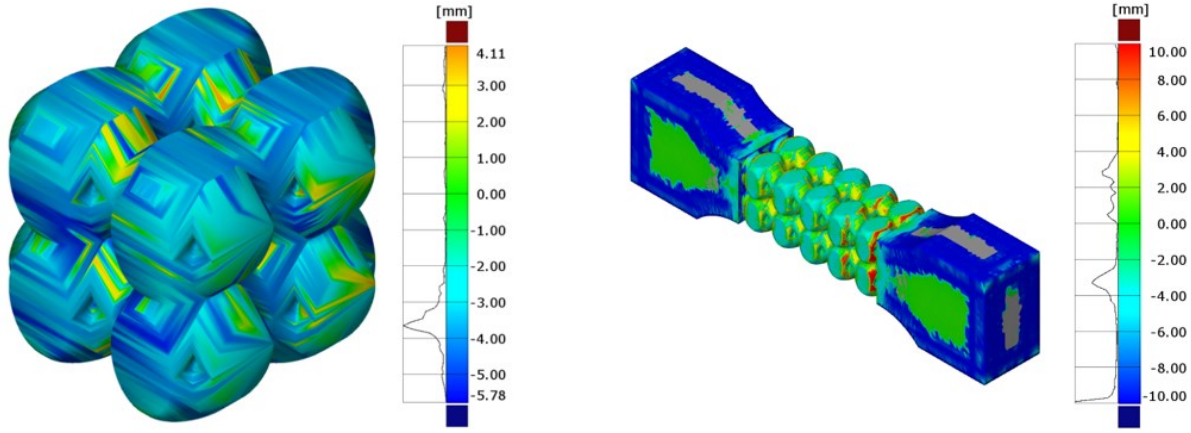

Figure 38. Shape deviation color map of 316L 70% compression and tension sample.

CHAPTER 5

CONCLUSIONS AND FUTURE WORK

5.1 Conclusions

The present work provides an original method to model and simulate bimetallic lattice structures, and some insight into the experimental porosity and shape deviation of the LPBF manufactured 316L and 17-4 PH samples. Bimetallic lattice structures are an emerging field of materials that harness the properties of two constituent materials and provide a metamaterial capable of engineered, functional response. The capability to engineer these metamaterials makes them an ideal candidate for applications in biomedical, aerospace, defence, space, and oil and gas industries. The bimetallic composite combination studied and modeled in this work also possesses functional properties due to the dissolvable aluminum alloy matrix, which allows the composite to dissolve partially while retaining its cellular, lattice-based stainless steel structure. The compressive and tensile behaviour of 316L stainless steel lattice, bulk dissolvable aluminum alloy, and 316L stainless steel/dissolvable aluminum bimetallic composite were tested and simulated via finite element analysis, and the following conclusions are obtained:

1. The developed FEA model is able to recast the experimental results. After validating the effectiveness of ABAQUS™ FEA simulation on the current experiments, FEA simulation can be used to explore different volume fractions of base lattice and filler to obtain desired properties without further experiments. For bulk and lattice samples, the average deviations between experimental and FEA results are 9.8% and 5.0% for yield stress and ultimate stress in compression, and 2.1% and 8.9% in tension, respectively. For composite samples, the average deviations

between experimental and FEA results are 2.0% for ultimate stress are 2.0%in both compression and tension. Further improvements to the FEA model can be made by integrating the manufacturing dimensional variations as well as manufacturing induced material imperfections into the geometry and material models.

2. 316L stainless steel has better compressive properties and higher resistance to the tensile loading than dissolvable aluminum alloy. The latter is more brittle with less elongation.

3. In the tension test, due to lack of bonding, the load does not transfer much from the 316L stainless steel lattice to aluminum alloy. However, the aluminum alloy matrix plays an indispensable role in the compression test and enhances the compression strength of the composite in comparison to the lattice itself.

4. The elastic modulus, yield stress, and ultimate stress of both the 316L stainless steel lattice and bimetallic composite were lower than the bulk aluminum, indicating that the performance of the lattice and composite with a volume fraction of 28.82% of lattice material is still not that satisfactory. Increasing the strut diameter of lattice to achieve a higher volume fraction is expected to enhance the mechanical properties, including both compressive and tensile strengths.

Besides, LPBF process is gradually shifting gears from a prototyping technology to a production scale industrial manufacturing system. The applicability of the process in various applications demand an investigation into the output part properties posing an intrinsic challenge of the process. Lattice structures with different volume fractions were utilized to investigate the effect of the geometric changes on the porosity and shape deviation. Database accumulated can be used by researchers and industries for quantifying the porosity and compensating the shape deviation or shrinkage for LPBF of 316L and 17-4 PH material.

5.2 Future Work

The present work is part of an ongoing research where effort will be made continually to analyze the samples further to build the relationship between mechanical properties and microstructure. Experimental analysis has been conducted with DIC and CT microscopy in this study to explore mechanical properties and geometric deviation of lattice structures. However, the effect of material on the lattice structure was studied only with 316L stainless steel, 17-4PH stainless steel and aluminum alloy. Besides, as mentioned before, mechanical properties such as strength and stiffness can be enhanced by optimizing the unit cell structure, or increasing the volume fraction of the lattice material. Thus, future research can be focused on the following directions:

1. Further investigation can be performed for specimens with the same dimensions as outlined in the ASTM standard and unit cell lattice with different materials. For example, an experimental comparison of the strength of lattice structure between 316L stainless steel, 17-4PH stainless steel and duplex stainless steel is valuable to be conducted.
2. The unit cell of lattice structures can be optimized by modifying the structure of the unit cell, enlarging the strut diameter, or increasing the density of the unit cell arrangement in the lattice, which will improve the strength of the structure.
3. The FEA model can be further optimized by combining various element types. Mesh can be generated more flexibly using other mesh-creating software and then imported into Abaqus for stress and strain simulation instead of automatically generating mesh by Abaqus itself, which will apparently improve the simulation accuracy.
4. The process parameters of the LPBF process need to consider both mechanical and geometric properties of the component to be manufactured and further optimized to minimize the shrinkage of struts. Thus, the experimental strength tested on specimens is

expected to increase, which will better match the FEA results based on the nominal models without built-in defects and imperfections.

5. Such database from X-ray tomography and deviation analysis are required for other materials as well with different geometric shapes, sizes, and process parameters to complement the process similar to machining and milling centers. It will not only make the process more reliable but will also help researchers to create design tools for predictive analysis and simulations.

Bibliography

1. Liu, L., Kamm, P., García-Moreno, F., Banhart, J., Pasini, D.: Elastic and failure response of imperfect three-dimensional metallic lattices: the role of geometric defects induced by Selective Laser Melting. J. Mech. Phys. Solids. 107, 160–184 (2017). https://doi.org/10.1016/j.jmps.2017.07.003

2. Dallago, M., Zanini, F., Carmignato, S., Pasini, D., Benedetti, M.: Effect of the geometrical defectiveness on the mechanical properties of SLM biomedical Ti6Al4V lattices. Procedia Struct. Integr. 13, 161–167 (2018). https://doi.org/10.1016/j.prostr.2018.12.027

3. El Elmi, A., Melancon, D., Asgari, M., Liu, L., Pasini, D.: Experimental and numerical investigation of selective laser melting-induced defects in Ti-6Al-4V octet truss lattice material: The role of material microstructure and morphological variations. J. Mater. Res. 1–13 (2020). https://doi.org/10.1557/jmr.2020.75

4. Dallago, M., Raghavendra, S., Luchin, V., Zappini, G., Pasini, D., Benedetti, M.: Geometric assessment of lattice materials built via Selective Laser Melting. Mater. Today Proc. 7, 353–361 (2019). https://doi.org/10.1016/j.matpr.2018.11.096

5. Sharma, P., Pandey, P.M.: Morphological and mechanical characterization of topologically ordered open cell porous iron foam fabricated using 3D printing and pressureless microwave sintering. Mater. Des. 160, 442–454 (2018). https://doi.org/10.1016/j.matdes.2018.09.029

6. Dressler, A.D., Jost, E.W., Miers, J.C., Moore, D.G., Seepersad, C.C., Boyce, B.L.: Heterogeneities dominate mechanical performance of additively manufactured metal lattice

struts. Addit. Manuf. 28, 692–703 (2019). https://doi.org/10.1016/j.addma.2019.06.011

7. Bagheri, Z.S., Melancon, D., Liu, L., Johnston, R.B., Pasini, D.: Compensation strategy to reduce geometry and mechanics mismatches in porous biomaterials built with Selective Laser Melting. J. Mech. Behav. Biomed. Mater. 70, 17–27 (2017). https://doi.org/10.1016/j.jmbbm.2016.04.041

8. Alsalla, H., Hao, L., Smith, C.: Fracture toughness and tensile strength of 316L stainless steel cellular lattice structures manufactured using the selective laser melting technique. Mater. Sci. Eng. A. 669, 1–6 (2016). https://doi.org/10.1016/j.msea.2016.05.075

9. Tsopanos, S., Mines, R.A.W., McKown, S., Shen, Y., Cantwell, W.J., Brooks, W., Sutcliffe, C.J.: The influence of processing parameters on the mechanical properties of selectively laser melted stainless steel microlattice structures. J. Manuf. Sci. Eng. Trans. ASME. 132, 0410111–04101112 (2010). https://doi.org/10.1115/1.4001743

10. Seepersad, C.C., Allison, J.A., Dressler, A.D., Boyce, B.L., Kovar, D.: An experimental approach for enhancing the predictability of mechanical properties of additively manufactured architected materials with manufacturing-induced variability. Elsevier Ltd (2020)

11. O.Rehme, C.Emmelmann, D.S.: Selective Laser Melting of lattice structures in solid shells. (1970)

12. Hengsbach, F., Koppa, P., Duschik, K., Holzweissig, M.J., Burns, M., Nellesen, J., Tillmann, W., Tröster, T., Hoyer, K.P., Schaper, M.: Duplex stainless steel fabricated by selective laser melting - Microstructural and mechanical properties. Mater. Des. 133, 136–142 (2017). https://doi.org/10.1016/j.matdes.2017.07.046

13. Köhnen, P., Haase, C., Bültmann, J., Ziegler, S., Schleifenbaum, J.H., Bleck, W.: Mechanical properties and deformation behavior of additively manufactured lattice structures of stainless steel. Mater. Des. 145, 205–217 (2018). https://doi.org/10.1016/j.matdes.2018.02.062

14. Zhong, T., He, K., Li, H., Yang, L.: Mechanical properties of lightweight 316L stainless steel lattice structures fabricated by selective laser melting. Mater. Des. 181, 108076 (2019). https://doi.org/10.1016/j.matdes.2019.108076

15. Yan, C., Hao, L., Hussein, A., Young, P., Raymont, D.: Advanced lightweight 316L stainless steel cellular lattice structures fabricated via selective laser melting. Mater. Des. 55, 533–541 (2014). https://doi.org/10.1016/j.matdes.2013.10.027

16. McKown, S., Shen, Y., Brookes, W.K., Sutcliffe, C.J., Cantwell, W.J., Langdon, G.S., Nurick, G.N., Theobald, M.D.: The quasi-static and blast loading response of lattice structures. Int. J. Impact Eng. 35, 795–810 (2008). https://doi.org/10.1016/j.ijimpeng.2007.10.005

17. Park, J.H., Park, K.: Compressive behavior of soft lattice structures and their application to functional compliance control. Addit. Manuf. 33, 101148 (2020). https://doi.org/10.1016/j.addma.2020.101148

18. Yánez, A., Herrera, A., Martel, O., Monopoli, D., Afonso, H.: Compressive behaviour of gyroid lattice structures for human cancellous bone implant applications. Mater. Sci. Eng. C. 68, 445–448 (2016). https://doi.org/10.1016/j.msec.2016.06.016

19. Kellogg, R.A., Russell, A.M., Lograsso, T.A., Flatau, A.B., Clark, A.E., Wun-Fogle, M.: Tensile properties of magnetostrictive iron-gallium alloys. Acta Mater. 52, 5043–5050

(2004). https://doi.org/10.1016/j.actamat.2004.07.007

20. Rossiter, J.D., Johnson, A.A., Bingham, G.A.: Assessing the Design and Compressive Performance of Material Extruded Lattice Structures. 3D Print. Addit. Manuf. 7, 19–27 (2020). https://doi.org/10.1089/3dp.2019.0030

21. Campanelli, S.L., Contuzzi, N., Ludovico, A.D., Caiazzo, F., Cardaropoli, F., Sergi, V.: Manufacturing and characterization of Ti6Al4V lattice components manufactured by selective laser melting. Materials (Basel). 7, 4803–4822 (2014). https://doi.org/10.3390/ma7064803

22. Geng, L., Wu, W., Sun, L., Fang, D.: Damage characterizations and simulation of selective laser melting fabricated 3D re-entrant lattices based on in-situ CT testing and geometric reconstruction. Int. J. Mech. Sci. 157–158, 231–242 (2019). https://doi.org/10.1016/j.ijmecsci.2019.04.054

23. Zargarian, A., Esfahanian, M., Kadkhodapour, J., Ziaei-Rad, S., Zamani, D.: On the fatigue behavior of additive manufactured lattice structures. Theor. Appl. Fract. Mech. 100, 225–232 (2019). https://doi.org/10.1016/j.tafmec.2019.01.012

24. Peng, C., Tran, P., Nguyen-Xuan, H., Ferreira, A.J.M.: Mechanical performance and fatigue life prediction of lattice structures: Parametric computational approach. Compos. Struct. 235, 111821 (2020). https://doi.org/10.1016/j.compstruct.2019.111821

25. Moongkhamklang, P., Deshpande, V.S., Wadley, H.N.G.: The compressive and shear response of titanium matrix composite lattice structures. Acta Mater. 58, 2822–2835 (2010). https://doi.org/10.1016/j.actamat.2010.01.004

26. De Wild, M., Ghayor, C., Zimmermann, S., Rüegg, J., Nicholls, F., Schuler, F., Chen, T.H., Weber, F.E.: Osteoconductive Lattice Microarchitecture for Optimized Bone Regeneration. 3D Print. Addit. Manuf. 6, 40–49 (2019). https://doi.org/10.1089/3dp.2017.0129

27. Egan, P., Wang, X., Greutert, H., Shea, K., Wuertz-Kozak, K., Ferguson, S.: Mechanical and Biological Characterization of 3D Printed Lattices. 3D Print. Addit. Manuf. 6, 73–81 (2019). https://doi.org/10.1089/3dp.2018.0125

28. Melancon, D., Bagheri, Z.S., Johnston, R.B., Liu, L., Tanzer, M., Pasini, D.: Mechanical characterization of structurally porous biomaterials built via additive manufacturing: experiments, predictive models, and design maps for load-bearing bone replacement implants. Acta Biomater. 63, 350–368 (2017). https://doi.org/10.1016/j.actbio.2017.09.013

29. Al-Ketan, O., Lee, D.W., Rowshan, R., Abu Al-Rub, R.K.: Functionally graded and multi-morphology sheet TPMS lattices: Design, manufacturing, and mechanical properties. J. Mech. Behav. Biomed. Mater. 102, 103520 (2020). https://doi.org/10.1016/j.jmbbm.2019.103520

30. Liu, F., Mao, Z., Zhang, P., Zhang, D.Z., Jiang, J., Ma, Z.: Functionally graded porous scaffolds in multiple patterns: New design method, physical and mechanical properties. Mater. Des. 160, 849–860 (2018). https://doi.org/10.1016/j.matdes.2018.09.053

31. Li, D., Liao, W., Dai, N., Dong, G., Tang, Y., Xie, Y.M.: Optimal design and modeling of gyroid-based functionally graded cellular structures for additive manufacturing. CAD Comput. Aided Des. 104, 87–99 (2018). https://doi.org/10.1016/j.cad.2018.06.003

32. Azzouz, L., Chen, Y., Zarrelli, M., Pearce, J.M., Mitchell, L., Ren, G., Grasso, M.: Mechanical properties of 3-D printed truss-like lattice biopolymer non-stochastic structures

for sandwich panels with natural fibre composite skins. Compos. Struct. 213, 220–230 (2019). https://doi.org/10.1016/j.compstruct.2019.01.103

33. Fan, H., Yang, W., Bin, W., Yan, Y., Qiang, F., Zhuang, Z.: TSINGHUA SCIENCE AND TECHNOLOGY I S S N 1 0 0 7 -0 2 1 4 0 4 / 1 8 p Design and Manufacturing of a Composite Lattice Structure Reinforced by Continuous Carbon Fibers. Tsinghua Sci. Technol. 5, 1–5 (2006)

34. Ye, G., Bi, H., Chen, L., Hu, Y.: Compression and Energy Absorption Performances of 3D Printed Polylactic Acid Lattice Core Sandwich Structures. 3D Print. Addit. Manuf. 6, 333–343 (2019). https://doi.org/10.1089/3dp.2019.0068

35. Arabnejad, S., Pasini, D.: Mechanical properties of lattice materials via asymptotic homogenization and comparison with alternative homogenization methods. Int. J. Mech. Sci. 77, 249–262 (2013). https://doi.org/10.1016/j.ijmecsci.2013.10.003

36. Wang, Y., Xu, H., Pasini, D.: Multiscale isogeometric topology optimization for lattice materials. Comput. Methods Appl. Mech. Eng. 316, 568–585 (2017). https://doi.org/10.1016/j.cma.2016.08.015

37. Andersen, M.N., Wang, F., Sigmund, O.: On the competition for ultimately stiff and strong architected materials. arXiv. (2020)

38. Alzahrani, M., Choi, S.K., Rosen, D.W.: Design of truss-like cellular structures using relative density mapping method. Mater. Des. 85, 349–360 (2015). https://doi.org/10.1016/j.matdes.2015.06.180

39. Ai, L., Gao, X.L.: Metamaterials with negative Poisson's ratio and non-positive thermal

expansion. Compos. Struct. 162, 70–84 (2017). https://doi.org/10.1016/j.compstruct.2016.11.056

40. Deng, F., Nguyen, Q.K., Zhang, P.: Multifunctional liquid metal lattice materials through hybrid design and manufacturing. Addit. Manuf. 33, 101117 (2020). https://doi.org/10.1016/j.addma.2020.101117

41. Nagesha, B.K., Dhinakaran, V., Varsha Shree, M., Manoj Kumar, K.P., Chalawadi, D., Sathish, T.: Review on characterization and impacts of the lattice structure in additive manufacturing. Mater. Today Proc. 21, 916–919 (2020). https://doi.org/10.1016/J.MATPR.2019.08.158

42. Zadpoor, A.A.: Mechanical performance of additively manufactured meta-biomaterials. Acta Biomater. 85, 41–59 (2019). https://doi.org/10.1016/J.ACTBIO.2018.12.038

43. Nazir, A., Abate, K.M., Kumar, A., Jeng, J.Y.: A state-of-the-art review on types, design, optimization, and additive manufacturing of cellular structures. Int. J. Adv. Manuf. Technol. 104, 3489–3510 (2019). https://doi.org/10.1007/s00170-019-04085-3

44. Maconachie, T., Leary, M., Lozanovski, B., Zhang, X., Qian, M., Faruque, O., Brandt, M.: SLM lattice structures: Properties, performance, applications and challenges. Mater. Des. 183, 108137 (2019). https://doi.org/10.1016/j.matdes.2019.108137

45. Contuzzi, N., Campanelli, S.L., Casavola, C., Lamberti, L.: Manufacturing and characterization of 18Ni marage 300 lattice components by selective laser melting. Materials (Basel). 6, 3451–3468 (2013). https://doi.org/10.3390/ma6083451

46. Hanzl, P., Zetková, I., Daňa, M.: Uniaxial tensile load of lattice structures produced by

metal additive manufacturing. Manuf. Technol. 19, 228–231 (2019). https://doi.org/10.21062/ujep/274.2019/a/1213-2489/mt/19/2/228

47. Li, C., Lei, H., Liu, Y., Zhang, X., Xiong, J., Zhou, H., Fang, D.: Crushing behavior of multi-layer metal lattice panel fabricated by selective laser melting. Int. J. Mech. Sci. 145, 389–399 (2018). https://doi.org/10.1016/j.ijmecsci.2018.07.029

48. Sola, A., Defanti, S., Mantovani, S., Merulla, A., Denti, L.: Technological Feasibility of Lattice Materials by Laser-Based Powder Bed Fusion of A357.0. 3D Print. Addit. Manuf. 7, 1–7 (2020). https://doi.org/10.1089/3dp.2019.0119

49. Peto, M., Ramirez-Cedillo, E., Uddin, M.J., Rodriguez, C.A., Siller, H.R.: Mechanical behavior of lattice structures fabricated by direct light processing with compression testing and size optimization of unit cells. ASME Int. Mech. Eng. Congr. Expo. Proc. 3, 1–10 (2019). https://doi.org/10.1115/IMECE2019-12260

50. Zhou, H., Cao, X., Li, C., Zhang, X., Fan, H., Lei, H., Fang, D.: Design of self-supporting lattices for additive manufacturing. J. Mech. Phys. Solids. 148, 104298 (2021). https://doi.org/10.1016/J.JMPS.2021.104298

51. Amani, Y., Dancette, S., Delroisse, P., Simar, A., Maire, E.: Compression behavior of lattice structures produced by selective laser melting: X-ray tomography based experimental and finite element approaches. Acta Mater. 159, 395–407 (2018). https://doi.org/10.1016/J.ACTAMAT.2018.08.030

52. Chen, Z., Wu, X., Tomus, D., Davies, C.H.J.: Surface roughness of Selective Laser Melted Ti-6Al-4V alloy components. Addit. Manuf. 21, 91–103 (2018). https://doi.org/10.1016/J.ADDMA.2018.02.009

53. Dallago, M., Winiarski, B., Zanini, F., Carmignato, S., Benedetti, M.: On the effect of geometrical imperfections and defects on the fatigue strength of cellular lattice structures additively manufactured via Selective Laser Melting. Int. J. Fatigue. 124, 348–360 (2019). https://doi.org/10.1016/J.IJFATIGUE.2019.03.019

54. Wang, D., Yang, Y., Yi, Z., Su, X.: Research on the fabricating quality optimization of the overhanging surface in SLM process. Int. J. Adv. Manuf. Technol. 65, 1471–1484 (2013). https://doi.org/10.1007/s00170-012-4271-4

55. Ghasri-Khouzani, M., Li, X., Bogno, A.A., Chen, Z., Liu, J., Henein, H., Qureshi, A.J.: Fabrication of aluminum/stainless steel bimetallic composites through a combination of additive manufacturing and vacuum-assisted melt infiltration casting. J. Manuf. Process. 69, 320–330 (2021). https://doi.org/10.1016/J.JMAPRO.2021.07.047

56. Yao, C., Xu, B., Zhang, X., Huang, J., Fu, J., Wu, Y.: Interface microstructure and mechanical properties of laser welding copper-steel dissimilar joint. Opt. Lasers Eng. 47, 807–814 (2009). https://doi.org/10.1016/j.optlaseng.2009.02.004

57. Abbasi, M., Karimi Taheri, A., Salehi, M.T.: Growth rate of intermetallic compounds in Al/Cu bimetal produced by cold roll welding process. J. Alloys Compd. 319, 233–241 (2001). https://doi.org/10.1016/S0925-8388(01)00872-6

58. Zareie Rajani, H.R., Akbari Mousavi, S.A.A.: The effect of explosive welding parameters on metallurgical and mechanical interfacial features of Inconel 625/plain carbon steel bimetal plate. Mater. Sci. Eng. A. 556, 454–464 (2012). https://doi.org/10.1016/j.msea.2012.07.012

59. Vendra, L.J., Rabiei, A.: A study on aluminum-steel composite metal foam processed by

casting. Mater. Sci. Eng. A. 465, 59–67 (2007). https://doi.org/10.1016/j.msea.2007.04.037

60. Viala, J.C., Peronnet, M., Barbeau, F., Bosselet, F., Bouix, J.: Interface chemistry in aluminium alloy castings reinforced with iron base inserts. Compos. Part A Appl. Sci. Manuf. 33, 1417–1420 (2002). https://doi.org/10.1016/S1359-835X(02)00158-6

61. Onuike, B., Bandyopadhyay, A.: Functional bimetallic joints of Ti6Al4V to SS410. Addit. Manuf. 31, 100931 (2020). https://doi.org/10.1016/j.addma.2019.100931

62. Sahasrabudhe, H., Harrison, R., Carpenter, C., Bandyopadhyay, A.: Stainless steel to titanium bimetallic structure using LENS^{TM}. Addit. Manuf. 5, 1–8 (2015). https://doi.org/10.1016/j.addma.2014.10.002

63. Anderson, R., Terrell, J., Schneider, J., Thompson, S., Gradl, P.: Characteristics of Bi-metallic Interfaces Formed During Direct Energy Deposition Additive Manufacturing Processing. Metall. Mater. Trans. B Process Metall. Mater. Process. Sci. 50, 1921–1930 (2019). https://doi.org/10.1007/s11663-019-01612-1

64. Banait, S.M., Paul, C.P., Jinoop, A.N., Kumar, H., Pawade, R.S., Bindra, K.S.: Experimental investigation on laser directed energy deposition of functionally graded layers of Ni-Cr-B-Si and SS316L. Opt. Laser Technol. 121, 105787 (2020). https://doi.org/10.1016/j.optlastec.2019.105787

65. Zhang, X., Sun, C., Pan, T., Flood, A., Zhang, Y., Li, L., Liou, F.: Additive manufacturing of copper – H13 tool steel bi-metallic structures via Ni-based multi-interlayer. Addit. Manuf. 36, 101474 (2020). https://doi.org/10.1016/j.addma.2020.101474

66. Demir, A.G., Previtali, B.: Multi-material selective laser melting of Fe/Al-12Si components.

Manuf. Lett. 11, 8–11 (2017). https://doi.org/10.1016/j.mfglet.2017.01.002

67. Tey, C.F., Tan, X., Sing, S.L., Yeong, W.Y.: Additive manufacturing of multiple materials by selective laser melting: Ti-alloy to stainless steel via a Cu-alloy interlayer. Addit. Manuf. 31, 100970 (2020). https://doi.org/10.1016/j.addma.2019.100970

68. Liu, Z.H., Zhang, D.Q., Sing, S.L., Chua, C.K., Loh, L.E.: Interfacial characterization of SLM parts in multi-material processing: Metallurgical diffusion between 316L stainless steel and C18400 copper alloy. Mater. Charact. 94, 116–125 (2014). https://doi.org/10.1016/j.matchar.2014.05.001

69. Mei, X., Wang, X., Peng, Y., Gu, H., Zhong, G., Yang, S.: Interfacial characterization and mechanical properties of 316L stainless steel/inconel 718 manufactured by selective laser melting. Mater. Sci. Eng. A. 758, 185–191 (2019). https://doi.org/10.1016/j.msea.2019.05.011

70. Zhang, M., Yang, Y., Wang, D., Song, C., Chen, J.: Microstructure and mechanical properties of CuSn/18Ni300 bimetallic porous structures manufactured by selective laser melting. Mater. Des. 165, 107583 (2019). https://doi.org/10.1016/j.matdes.2019.107583

71. Pawlowski, A.E., Cordero, Z.C., French, M.R., Muth, T.R., Keith Carver, J., Dinwiddie, R.B., Elliott, A.M., Shyam, A., Splitter, D.A.: Damage-tolerant metallic composites via melt infiltration of additively manufactured preforms. Mater. Des. 127, 346–351 (2017). https://doi.org/10.1016/j.matdes.2017.04.072

72. Cheng, J., Gussev, M., Allen, J., Hu, X., Moustafa, A.R., Splitter, D.A., Shyam, A.: Deformation and failure of PrintCast A356/316 L composites: Digital image correlation and finite element modeling. Mater. Des. 195, 109061 (2020).

https://doi.org/10.1016/j.matdes.2020.109061

73. Parab, N.D., Zhao, C., Cunningham, R., Escano, L.I., Gould, B., Wolff, S., Guo, Q., Xiong, L., Kantzos, C., Pauza, J., Fezzaa, K., Greco, A., Rollett, A., Chen, L., Sun, T.: High-speed Synchrotron X-ray Imaging of Laser Powder Bed Fusion Process. Synchrotron Radiat. News. 32, 4–8 (2019). https://doi.org/10.1080/08940886.2019.1582280

74. Li, X., Zhao, C., Sun, T., Tan, W.: Revealing transient powder-gas interaction in laser powder bed fusion process through multi-physics modeling and high-speed synchrotron x-ray imaging. Addit. Manuf. 35, 101362 (2020). https://doi.org/10.1016/j.addma.2020.101362

75. Sun, T.: Probing Ultrafast Dynamics in Laser Powder Bed Fusion Using High-Speed X-Ray Imaging: A Review of Research at the Advanced Photon Source. Jom. 72, 999–1008 (2020). https://doi.org/10.1007/s11837-020-04015-9

76. Parab, N., Zhao, C., Cunningham, R., Escano, L.I., Fezzaa, K., Rollett, A., Chen, L., Sun, T.: In situ Characterization of Laser Powder Bed Fusion Using High-Speed Synchrotron X-ray Imaging Technique . Microsc. Microanal. 25, 2566–2567 (2019). https://doi.org/10.1017/s1431927619013564

77. Kim, F.H., Moylan, S.P., Phan, T.Q., Garboczi, E.J.: Investigation of the Effect of Artificial Internal Defects on the Tensile Behavior of Laser Powder Bed Fusion 17–4 Stainless Steel Samples: Simultaneous Tensile Testing and X-Ray Computed Tomography. Exp. Mech. 60, 987–1004 (2020). https://doi.org/10.1007/s11340-020-00604-6

78. Ulbricht, A., Mohr, G., Altenburg, S.J., Oster, S., Maierhofer, C., Bruno, G.: Can potential defects in lpbf be healed from the laser exposure of subsequent layers? A quantitative study.

Metals (Basel). 11, 1–14 (2021). https://doi.org/10.3390/met11071012

79. Liu, L., Kamm, P., García-Moreno, F., Banhart, J., Pasini, D.: Elastic and failure response of imperfect three-dimensional metallic lattices: the role of geometric defects induced by Selective Laser Melting. J. Mech. Phys. Solids. 107, 160–184 (2017). https://doi.org/10.1016/J.JMPS.2017.07.003

80. Forien, J.B., Calta, N.P., DePond, P.J., Guss, G.M., Roehling, T.T., Matthews, M.J.: Detecting keyhole pore defects and monitoring process signatures during laser powder bed fusion: A correlation between in situ pyrometry and ex situ X-ray radiography. Addit. Manuf. 35, 101336 (2020). https://doi.org/10.1016/J.ADDMA.2020.101336

81. Hastie, J.C., Kartal, M.E., Carter, L.N., Attallah, M.M., Mulvihill, D.M.: Classifying shape of internal pores within AlSi10Mg alloy manufactured by laser powder bed fusion using 3D X-ray micro computed tomography: Influence of processing parameters and heat treatment. Mater. Charact. 163, 110225 (2020). https://doi.org/10.1016/j.matchar.2020.110225

82. Best, J.P., Ostergaard, H.E., Li, B., Stolpe, M., Yang, F., Nomoto, K., Hasib, M.T., Muránsky, O., Busch, R., Li, X., Kruzic, J.J.: Fracture and fatigue behaviour of a laser additive manufactured Zr-based bulk metallic glass. Addit. Manuf. 36, 101416 (2020). https://doi.org/10.1016/j.addma.2020.101416

83. Kim, F.H., Pintar, A.L., Moylan, S.P., Garboczi, E.J.: The influence of X-Ray computed tomography acquisition parameters on image quality and probability of detection of additive manufacturing defects. J. Manuf. Sci. Eng. Trans. ASME. 141, 1–11 (2019). https://doi.org/10.1115/1.4044515

84. Du Plessis, A., Yadroitsev, I., Yadroitsava, I., Le Roux, S.G.: X-Ray Microcomputed

Tomography in Additive Manufacturing: A Review of the Current Technology and Applications. 3D Print. Addit. Manuf. 5, 227–247 (2018). https://doi.org/10.1089/3dp.2018.0060

85. Moran, T.P., Warner, D.H., Soltani-Tehrani, A., Shamsaei, N., Phan, N.: Spatial inhomogeneity of build defects across the build plate in laser powder bed fusion. Addit. Manuf. 47, 102333 (2021). https://doi.org/10.1016/j.addma.2021.102333

86. Kim, F.H., Pintar, A.L., Fox, J., Donmez, A.M.: PROBABILITY OF DETECTION OF X-RAY COMPUTED TOMOGRAPHY OF ADDITIVE MANUFACTURING DEFECTS. 1–3 (2019)

87. Baier, M., Sinico, M., Witvrouw, A., Dewulf, W., Carmignato, S.: A novel tomographic characterisation approach for sag and dross defects in metal additively manufactured channels. Addit. Manuf. 39, 101892 (2021). https://doi.org/10.1016/j.addma.2021.101892

88. Parab, N.D., Zhao, C., Cunningham, R., Escano, L.I., Fezzaa, K., Everhart, W., Rollett, A.D., Chen, L., Sun, T.: Ultrafast X-ray imaging of laser–metal additive manufacturing processes. J. Synchrotron Radiat. 25, 1467–1477 (2018). https://doi.org/10.1107/S1600577518009554

89. Guo, Q., Zhao, C., Escano, L.I., Young, Z., Xiong, L., Fezzaa, K., Everhart, W., Brown, B., Sun, T., Chen, L.: Transient dynamics of powder spattering in laser powder bed fusion additive manufacturing process revealed by in-situ high-speed high-energy x-ray imaging. Acta Mater. 151, 169–180 (2018). https://doi.org/10.1016/j.actamat.2018.03.036

90. Zhao, C., Fezzaa, K., Cunningham, R.W., Wen, H., De Carlo, F., Chen, L., Rollett, A.D., Sun, T.: Real-time monitoring of laser powder bed fusion process using high-speed X-ray

imaging and diffraction. Sci. Rep. 7, 1–11 (2017). https://doi.org/10.1038/s41598-017-03761-2

91. Bobel, A., Hector, L.G., Chelladurai, I., Sachdev, A.K., Brown, T., Poling, W.A., Kubic, R., Gould, B., Zhao, C., Parab, N., Greco, A., Sun, T.: In situ synchrotron X-ray imaging of 4140 steel laser powder bed fusion. Materialia. 6, 100306 (2019). https://doi.org/10.1016/j.mtla.2019.100306

92. Kouraytem, N., Chiang, P.J., Jiang, R., Kantzos, C., Pauza, J., Cunningham, R., Wu, Z., Tang, G., Parab, N., Zhao, C., Fezzaa, K., Sun, T., Rollett, A.D.: Solidification crack propagation and morphology dependence on processing parameters in AA6061 from ultra-high-speed x-ray visualization. Addit. Manuf. 42, 101959 (2021). https://doi.org/10.1016/j.addma.2021.101959

93. Shamsujjoha, M., Agnew, S.R., Fitz-Gerald, J.M., Moore, W.R., Newman, T.A.: High Strength and Ductility of Additively Manufactured 316L Stainless Steel Explained. Metall. Mater. Trans. A Phys. Metall. Mater. Sci. 49, 3011–3027 (2018). https://doi.org/10.1007/s11661-018-4607-2

94. Xu, W., Yu, A., Lu, X., Tamaddon, M., Wang, M., Zhang, J., Zhang, J., Qu, X., Liu, C., Su, B.: Design and performance evaluation of additively manufactured composite lattice structures of commercially pure Ti (CP–Ti). Bioact. Mater. 6, 1215–1222 (2021). https://doi.org/10.1016/j.bioactmat.2020.10.005

95. McDonald-Wharry, J., Amirpour, M., Pickering, K.L., Battley, M., Fu, Y.: Moisture sensitivity and compressive performance of 3D-printed cellulose-biopolyester foam lattices. Addit. Manuf. 40, 101918 (2021). https://doi.org/10.1016/j.addma.2021.101918

96. Mahmoud, D., Al-Rubaie, K.S., Elbestawi, M.A.: The influence of selective laser melting defects on the fatigue properties of Ti6Al4V porosity graded gyroids for bone implants. Int. J. Mech. Sci. 193, (2021). https://doi.org/10.1016/j.ijmecsci.2020.106180

97. Feng, J., Liu, B., Lin, Z., Fu, J.: Isotropic octet-truss lattice structure design and anisotropy control strategies for implant application. Mater. Des. 203, 109595 (2021). https://doi.org/10.1016/j.matdes.2021.109595

98. Traxel, K.D., Groden, C., Valladares, J., Bandyopadhyay, A.: Mechanical properties of additively manufactured variable lattice structures of Ti6Al4V. Mater. Sci. Eng. A. 809, 140925 (2021). https://doi.org/10.1016/j.msea.2021.140925

99. Hajjari, M., Jafari Nedoushan, R., Dastan, T., Sheikhzadeh, M., Yu, W.R.: Lightweight weft-knitted tubular lattice composite for energy absorption applications: An experimental and numerical study. Int. J. Solids Struct. 213, 77–92 (2021). https://doi.org/10.1016/j.ijsolstr.2020.12.017

100. Li, P.Y., Ma, Y.E., Sun, W.B., Qian, X., Zhang, W., Wang, Z.H.: Fracture and failure behavior of additive manufactured Ti6Al4V lattice structures under compressive load. Eng. Fract. Mech. 244, (2021). https://doi.org/10.1016/j.engfracmech.2021.107537

101. Cao, X., Xiao, D., Li, Y., Wen, W., Zhao, T., Chen, Z., Jiang, Y., Fang, D.: Dynamic compressive behavior of a modified additively manufactured rhombic dodecahedron 316L stainless steel lattice structure. Thin-Walled Struct. 148, 106586 (2020). https://doi.org/10.1016/j.tws.2019.106586

102. Xiao, L., Song, W., Xu, X.: Experimental study on the collapse behavior of graded Ti-6Al-4V micro-lattice structures printed by selective laser melting under high speed impact. Thin-

Walled Struct. 155, 106970 (2020). https://doi.org/10.1016/j.tws.2020.106970

103. Goodall, R., Hernandez-Nava, E., Jenkins, S.N.M., Sinclair, L., Tyrwhitt-Jones, E., Khodadadi, M.A., Ip, D.H., Ghadbeigi, H.: The effects of defects and damage in the mechanical behavior of ti6al4v lattices. Front. Mater. 6, 1–11 (2019). https://doi.org/10.3389/fmats.2019.00117

104. Liu, F., Zhang, D.Z., Zhang, P., Zhao, M., Jafar, S.: Mechanical properties of optimized diamond lattice structure for bone scaffolds fabricated via selective laser melting. Materials (Basel). 11, (2018). https://doi.org/10.3390/ma11030374

105. Xiao, L., Song, W.: Additively-manufactured functionally graded Ti-6Al-4V lattice structures with high strength under static and dynamic loading: Experiments. Int. J. Impact Eng. 111, 255–272 (2018). https://doi.org/10.1016/j.ijimpeng.2017.09.018

106. Montanini, R., Rossi, G., Quattrocchi, A., Alizzio, D., Capponi, L., Marsili, R., Giacomo, A. Di, Tocci, T.: Structural characterization of complex lattice parts by means of optical non-contact measurements. I2MTC 2020 - Int. Instrum. Meas. Technol. Conf. Proc. 1–6 (2020). https://doi.org/10.1109/I2MTC43012.2020.9128771

107. Hao, W., Liu, Y., Wang, T., Guo, G., Chen, H., Fang, D.: Failure analysis of 3D printed glass fiber/PA12 composite lattice structures using DIC. Compos. Struct. 225, 111192 (2019). https://doi.org/10.1016/j.compstruct.2019.111192

108. Fíla, T., Koudelka, P., Falta, J., Zlámal, P., Rada, V., Adorna, M., Bronder, S., Jiroušek, O.: Dynamic impact testing of cellular solids and lattice structures: Application of two-sided direct impact Hopkinson bar. Int. J. Impact Eng. 148, (2021). https://doi.org/10.1016/j.ijimpeng.2020.103767

109. Li, S., Hu, M., Xiao, L., Song, W.: Compressive properties and collapse behavior of additively-manufactured layered-hybrid lattice structures under static and dynamic loadings. Thin-Walled Struct. 157, 107153 (2020). https://doi.org/10.1016/j.tws.2020.107153

110. ABAQUS: Abaqus 6.14. Abaqus 6.14 Anal. User's Guid. 14 (2014)

111. Mower, T.M., Long, M.J.: Mechanical behavior of additive manufactured, powder-bed laser-fused materials. Mater. Sci. Eng. A. 651, 198–213 (2016). https://doi.org/10.1016/j.msea.2015.10.068

112. Printer, M., Components, P.: CREATOR 3D Metal Printer for Precision Components.